

INFORMATION TO USERS

This manuscript has been reproduced from the microfilm master. UMI films the text directly from the original or copy submitted. Thus, some thesis and dissertation copies are in typewriter face, while others may be from any type of computer printer.

The quality of this reproduction is dependent upon the quality of the copy submitted. Broken or indistinct print, colored or poor quality illustrations and photographs, print bleedthrough, substandard margins, and improper alignment can adversely affect reproduction.

In the unlikely event that the author did not send UMI a complete manuscript and there are missing pages, these will be noted. Also, if unauthorized copyright material had to be removed, a note will indicate the deletion.

Oversize materials (e.g., maps, drawings, charts) are reproduced by sectioning the original, beginning at the upper left-hand corner and continuing from left to right in equal sections with small overlaps. Each original is also photographed in one exposure and is included in reduced form at the back of the book.

Photographs included in the original manuscript have been reproduced xerographically in this copy. Higher quality 6" x 9" black and white photographic prints are available for any photographs or illustrations appearing in this copy for an additional charge. Contact UMI directly to order.

U·M·I

University Microfilms International
A Bell & Howell Information Company
300 North Zeeb Road, Ann Arbor, MI 48106-1346 USA
313/761-4700 800/521-0600

Order Number 1349011

**Theoretical investigation of charge transfer process in
atom-surface scattering**

Berk, Murat Osman, M.A.

Rice University, 1992

U·M·I

**300 N. Zeeb Rd.
Ann Arbor, MI 48106**

RICE UNIVERSITY

**Theoretical Investigation of Charge Transfer
Process in Atom-Surface Scattering**

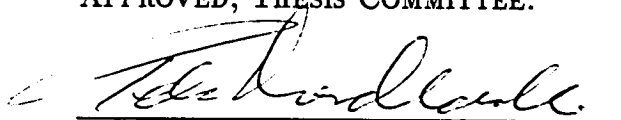
by

Murat O. Berk

A THESIS SUBMITTED
IN PARTIAL FULFILLMENT OF THE
REQUIREMENTS FOR THE DEGREE

Master of Arts

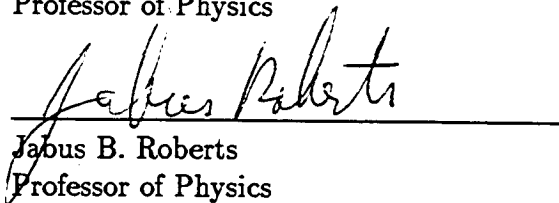
APPROVED, THESIS COMMITTEE:

A handwritten signature in dark ink, appearing to read "Peter Nordlander", is written over a horizontal line.

Peter Nordlander, Director
Assistant Professor of Physics

A handwritten signature in dark ink, appearing to read "J. P. Hannon", is written over a horizontal line.

James P. Hannon
Professor of Physics

A handwritten signature in dark ink, appearing to read "Jabus B. Roberts", is written over a horizontal line.

Jabus B. Roberts
Professor of Physics

Houston, Texas

April, 1992

ABSTRACT

Theoretical Investigation of Charge Transfer Process in Atom-Surface Scattering

by

Murat O. Berk

We present calculations of the lifetime broadening and the shifts of hydrogen atomic levels (both ground and excited levels) near impurity covered jellium metal surfaces using complex scaling technique. The impurities which are used in the calculations are Na, Cl and Cs. It has long been known, that the presence of the impurities on metal surfaces can both shift position and change the widths of the electronic levels. It is shown that for an accurate description of the system it is important to use support basis functions centered on the impurity.

We also investigate the accuracy of a classical treatment of electron transfer in atom metal collisions and compare it to Monte Carlo based quantum mechanical calculations. It is shown that for slow particles the treatments deviate from each other, thus giving different predictions for the sticking effects on the surface.

Acknowledgments

I would like to thank, my advisor, Dr. Peter Nordlander for his enormous technical and moral support. I should thank Dr. Hannon and Dr. Roberts for serving on my thesis committee.

I am grateful to my family. I would like to thank my wife Meral for her support, encouragement and for the environment she created for my studies since our first meeting. I would like to thank my dearest mother, Esin Berk and my dearest father Yasar Berk for their infinite support, encouragement and help in my education and life. Finally, I would like to express my dearest thanks to my brother Levent.

Contents

Abstract	ii
Acknowledgments	iii
List of Illustrations	vi
List of Tables	vii
1 Introduction	1
2 Theoretical description of the metal surface	3
2.1 Theory of self consistent surface potentials	3
2.1.1 Density Functional Formalism	3
2.1.2 Two regimes of approximation	6
2.1.3 Replacing an ionic lattice with uniform background	9
2.2 Theoretical description of the interaction between atom and surfaces .	12
3 Tunneling rates near surfaces	17
3.1 Calculation of Resonance States of Atoms near Metal Surfaces in the presence of Impurities	18
3.1.1 Calculation of the potential	19
3.1.2 Calculation of the shifts of atomic levels near surfaces using complex scaling	23
3.2 Two-centered basis functions and complex scaling	28
3.2.1 Geometry of the problem	29
3.2.2 Calculation of the matrix elements of the Hamiltonian	30

3.2.3	Addition of the impurity-based basis set	33
3.3	Results of the two centered complex scaling method	36
3.3.1	Results for the excited states of H on Na/Al	40
3.3.2	Results for the ground state(1s) of H on Na/Al	45
3.3.3	Results for Cl states	47
3.3.4	Results for Cs states	48
3.4	Discussion of the results	52
4	Dynamics of Charge Transfer	54
4.1	Dynamics of the charge transfer in Atom surface collisions in classical treatment	55
4.2	Dynamics of the charge transfer in atom surface collisions in the Quantum Mechanical picture	62
A	Derivation of force equations from potentials	67
B	Geometry of the problem	69
C	Impurity basis-function set	71
C.1	Definition of the basis set	71
C.2	Derivative of the radial part of the impurity basis-functions	72
C.3	Derivatives of the Impurity basis-functions w.r.t. Hydrogen center . .	72
D	Calculation of Hamiltonian	74
	Bibliography	77

Illustrations

2.1	Background and electronic charge densities near surfaces	11
2.2	Image, repulsive and van der Waals potentials for a clean Aluminium surface in a.u.	15
3.1	Contour of Cs potential on Al surface	27
3.2	Geometry of the problem	30
3.3	The convergence of different basis-function sets at adsorbate center with the existence of s basis-functions on the impurity center	38
3.4	Angular distribution of the potential as seen from the impurity center	41
3.5	s- and p-type basis-functions at the impurity center	42
3.6	H/Na/Al Results for n=2 m=0 states	43
3.7	H/Na/Al results for n=1 state	46
3.8	H/Cl/Al Results for n=2 m=0 state	46
3.9	H/Cs/Al Results for n=2 m=0 state	49
3.10	The probability distributions of the n=2 levels of H on Cs/Al	50
4.1	Charge transfer from the metal surface to the atom	57
4.2	Charge transfer probabilities for the ionization levels.	59
4.3	Charge transfer probabilities for the affinity levels.	59
4.4	The comparison for the charge transfer characteristics of SCA and MC simulations	66

Tables

4.1	The comparison of the charge transfer for SCA and MC simulations for 100K	64
4.2	The comparison of the charge transfer for SCA and MC simulations for 300K	64

Chapter 1

Introduction

The energies and lifetimes of excited states of atoms and molecules near metal surfaces are controlling factors in many dynamical phenomena at surfaces. Photochemistry at surfaces depends on the enhanced reactivity of electronically excited species and on the lifetime of the excitation.[1] Distributions of spatial position, velocity, charge and electronic states of sputtered particles depend strongly on the lifetimes of the electronic states.[2, 3] In the spectroscopy of adsorbed species, the lifetimes of excited states contribute to the broadening of adsorption peaks.[4] Lifetimes and energies of the excited states also determine survival probabilities of excited species in atom or molecule-surface scattering experiments.[5]

Most theoretical calculations of tunneling probabilities have so far ignored effects of coadsorbed impurities and assumed infinite planar surfaces. In a series of chemisorption calculations [6, 7], it has been shown that the electron potential outside a metal surface can be strongly influenced by electropositive or electronegative impurities. Such an influence will modify the shifts and broadenings of the electronic states of atoms, incident onto the surface.

The first calculation of energy level shifts and lifetime broadenings of the electronic levels of a hydrogen atom taking into account a realistic model of the impurity-induced fields was done by Nordlander and Lang [8]. In this calculation, a limited

basis centered only on the H was used. This approach failed to describe the shifts and broadenings of atoms like K and Cs, systems of fundamental importance in experiments.

In this thesis, an accurate multi-centered basis-function technique for the description of strong impurities is developed. We will present this technique and compare the lifetimes and energy shifts of the H levels with the previous calculations with the present calculations for the impurities Na and Cl. In addition to this, the shifts and broadenings of the excited H levels for Cs covered aluminium surfaces and the shifts and broadenings of the H ground state for Na covered aluminium surfaces are given.

These energy shifts and lifetimes can be used in dynamical calculations to describe the charge transfer process between the surface and atomic energy levels. These probabilities are first calculated by the time dependent Anderson model by Blandin. Later, other methods are suggested to describe single- or multi-level charge transfer processes.

In all of the classical models of charge transfer, fractional charges are allowed to exist on the atomic levels. The existence of fractional charges is not a truly quantum mechanical description of the electronic states of the atoms. Therefore, we develop a Monte Carlo based method for the calculation of the charge transfer rates. We then compare the classical treatment of the charge transfer to the Monte Carlo based one.

Chapter 2

Theoretical description of the metal surface

2.1 Theory of self consistent surface potentials

In order to calculate the electronic structure of metal surfaces we need a procedure that describes large and strongly inhomogeneous systems of electrons. Methods which have been used in the past are Thomas-Fermi [9] and Hartree methods. The most accurate theories for the inhomogeneous gases are based on Density Functional Theory. This method was introduced first by Hohenberg, Kohn and Sham [10] [11]. The basis of this theory is the density distribution of the electrons. The basic theorem in the density functional formalism states that the properties of the system, in particular the ground state of the energy, are functionals of this quantity. The energy of the system can be obtained from the variational principle where the electron density is the varied function.

2.1.1 Density Functional Formalism

In this section we describe the Hohenberg and Kohn formalism . We consider a system of electrons moving in a static potential $v(\vec{r})$. If we denote the kinetic energy with T , the electron-electron interaction with U and the electron external potential

interaction with V , we can write the second quantized Hamiltonian as

$$H = T + U + V \quad (2.1)$$

The ground state wavefunction for the electrons is Ψ , the related electron density is $n(\vec{r})$ and the number of the particles are given by

$$N = \int n(\vec{r}) d\vec{r}. \quad (2.2)$$

The ground state energy is E_N . The variational theorem states that $\langle \Psi' | H | \Psi' \rangle$ is a minimum when Ψ' is equal to Ψ if Ψ' corresponds to the same number of particles N .

$v(\vec{r})$ is a unique functional of $n(\vec{r})$ except for an additive constant. The uniqueness can be proven very easily by assuming the existence of another $v'(\vec{r})$ which gives rise to the same charge density $n(\vec{r})$. Calculating the Hamiltonian and interchanging the primed and unprimed variables leads to the inconsistency in the energy as $[E_N + E'_N < E'_N + E_N]$. Hence the potential $v(\vec{r})$ can be uniquely determined from the charge density functional. Thus $v(\vec{r})$ effectively modifies H and H determines a new Ψ ($n(\vec{r}) = |\Psi|^2$). Therefore the charge density can be calculated by iteration. A new potential can be calculated from this charge distribution, which in turn gives another charge distribution. This procedure can be repeated until self consistency is reached.

If we define a general energy functional in the form

$$E_v[n] = \int v(\vec{r}) n(\vec{r}) d\vec{r} + F[n] \quad (2.3)$$

where we can write $F[n]$ as

$$F[n] = \langle \Psi | T + U | \Psi \rangle \quad (2.4)$$

then the correct $n(\vec{r})$ with its well defined $v(\vec{r})$ is the one which gives spatial integral N and has $E_v[n]$ equal to the ground state energy E_N .

Separation of Electronic Terms

Since the Coulomb interactions are long-ranged we can separate them from $F[n]$, thus our energy functional takes the form

$$E_v[n] = \int v(\vec{r})n(\vec{r})d\vec{r} + \frac{1}{2} \int \frac{n(\vec{r})n(\vec{r}')}{r - r'} d\vec{r}d\vec{r}' + G[n] \quad (2.5)$$

where $G[n]$ is universal functional. The electrostatic potential can be written as

$$\Phi(\vec{r}) = v(\vec{r}) + \int \frac{n(\vec{r}')}{r - r'} d\vec{r}' \quad (2.6)$$

If we think of $v(\vec{r})$ as being due to distribution of positive charge density $n_+(\vec{r})$ our potential becomes

$$\Phi(\vec{r}) = \int \frac{n(\vec{r}') - n_+(\vec{r}')}{|\vec{r} - \vec{r}'|} d\vec{r}' \quad (2.7)$$

which can expressed in a different form as

$$\nabla^2 \Phi(\vec{r}) = -4\pi[n(\vec{r}) - n_+(\vec{r})] \quad (2.8)$$

We can also use a Lagrange multiplier form of the energy with multiplier μ , which is going to be our definition for chemical potential.

$$\delta \left\{ E_v[n] - \mu \int n(\vec{r})d\vec{r} \right\} \quad (2.9)$$

where μ is determined by 2.2, implies with the above equation that for correct charge density

$$\delta E_v[n]/\delta n(\vec{r}) = \mu \quad (2.10)$$

2.1.2 Two regimes of approximation

The problem of determining the ground-state energy and density for a many electron-system can be reduced to minimization of a functional of the density. The full complexity of the problem lies in determination of the form of $G[n]$. For the homogeneous system the solution for the Density Functional Theory is exact. In the perturbed systems, there are two regimes of interest. In the first case, the density is nearly constant but it may have rapid oscillations in space of small magnitude. In this case it is convenient to expand the charge density in a series in the deviation from constancy. In the second case the charge density exhibits slow variations from the constancy and these variations can be large. In this case we can expand the charge density in its gradients.

Gas near constant density

The density of the electrons can be written as a constant plus a varying disturbance which has zero spatial average

$$n(\vec{r}) = \bar{n} + \tilde{n}(\vec{r}) \quad (2.11)$$

If the charge density is almost constant (although it may have rapid oscillations), the $\tilde{n}(\vec{r})$ term is small and $G[n]$ can be expanded as

$$G[n] = G[\bar{n}] + \int K(|\vec{r} - \vec{r}'|) \tilde{n}(\vec{r}) \tilde{n}(\vec{r}') d\vec{r} d\vec{r}' + O(\tilde{n}^3) \quad (2.12)$$

The zeroth order term is known from studies of the uniform electron gas. The first order term is zero because the spatial average of $\tilde{n}(\vec{r})$ is zero. Hohenberg and Kohn

analyzed the second term and found that $K(\vec{r})$ is the inverse Fourier transform of $K(q)$, where $K(q)$ is given by

$$K(q) = (2\pi/q^2)[\epsilon(q) - 1]^{-1} \quad (2.13)$$

and where $\epsilon(q)$ is the static dielectric constant of the electron gas with a density \bar{n} . $K(q)$ has singularities (in the form $(q - 2k_F) \log(q - 2k_F)$) because of the sharpness of Fermi surface near $q = 2k_F$. The inverse Fourier transform of $K(q)$ shows long range oscillatory behavior where

$$\lim_{r \rightarrow \infty} K(\vec{r}) \approx \cos(2k_F r)/r^3 \quad (2.14)$$

which are the Friedel oscillations in the charge screening a disturbance in the electron gas. These oscillations occur in the vicinity of the impurities in the electron gas and near the metal surfaces which are our primary interest. For a proper description of the surface electronic structure it is crucial to include these Friedel oscillations. For the case in which $n(\vec{r})$ is not only small but slowly varying, $K(q)$ can be expanded around $q=0$

$$K(q) = a(\bar{n}) + b(\bar{n})q^2 + \dots \quad (2.15)$$

In this expansion $K(q)$ is a function of q^2 alone because of the isotropy of the electron gas. Up to this point, our analysis is exact. If we take only the first term in 2.15 we get the Thomas-Fermi method and if we take more terms we get extensions of this method. None of these solutions give rise to Friedel oscillations.

Gas of slowly varying density

For the case of slowly varying density we can express $G[n]$ as a function of a series of density gradients. Since the first gradient of $n(\mathbf{r})$ disappears we need only two coefficients until third order. $G[n]$ can be written as:

$$G[n] = \int d\vec{r} [g_0(n(\vec{r})) + g_2(n(\vec{r})) |\lambda n(\vec{r})|^2 + \dots] \quad (2.16)$$

The zeroth order term is just the energy density without electrostatic terms (Eqn.2.5).

We can define explicitly what is included in $g_0(n(\vec{r}))$.

$$g_0(n) = [t(n) + \epsilon_x(n) + \epsilon_c(n)]n \quad (2.17)$$

where $t(n)$ and $\epsilon_x(n)$ are defined in Hartree-Fock theory ($t(n) = 1.105/r_s(n)^2$ and $\epsilon_x(n) = -0.458/r_s(n)$). The correlation term is studied in literature and the simplest form is from Wigner and Pines [12],

$$\epsilon_c(n) = -0.44/[r_s(n) + 7.8] \quad (2.18)$$

The more appropriate form for high densities is

$$\epsilon_c(n) = 0.031 \log r_s(n) - 0.048 \quad (2.19)$$

For the g_2 term there exist many different approaches and Sham and Ortenburger [13] gives it as

$$g_2(n) = (72n)^{-1} + 0.00167n^{-4/3}114. \quad (2.20)$$

Work function

One of the important properties of the ground state charge distribution at the metal surfaces is the *work function*. It is defined as the minimum work required to remove

one electron from the metal to the infinity,

$$\Phi = [\phi(\infty) + E_{N-1}] - E_N. \quad (2.21)$$

where E_{N-1} is the ground state energy of the $N-1$ electrons, one being taken to infinity.

Using the definition of the chemical potential, the work function can be rewritten as

$$\Phi = \Delta\Phi - \bar{\mu}, \quad (2.22)$$

where

$$\Delta\Phi = \phi(\infty) - \bar{\phi}. \quad (2.23)$$

This can be thought of as dividing Φ into bulk ($-\bar{\mu}$) and surface ($\Delta\Phi$) components. All many-body effects are contained in the exchange and correlation contribution to the $\bar{\mu}$ and in their effect on the barrier potential $\Delta\phi$. The image force effect on ϕ may be regarded as contained in the disappearance of the correlation energy when the electron is moved away from the metal surface.

2.1.3 Replacing an ionic lattice with uniform background

It is known that, the interplanar spacing between layers is approximately the same, both in the interior of the bulk and at the surfaces (particularly for the densely packed crystal faces). Therefore the theory described above can be extended to approximate the behavior of the charge density near the metal surfaces. In the following discussions $n(\vec{r})$ is taken as conduction electron density and $v(\vec{r})$ is taken as contribution of nuclei and core electrons.

The self consistent calculations for $n(\vec{r})$ at the metal surface employs the model in which all the ions and the core electrons are replaced by a positive background of

a constant charge density. This is the so called *jellium model*. In an infinite crystal, the wavefunctions are plane-waves, which give rise to a uniform charge density. This model is appropriate for the so called simple metals, where the conduction band of the metal is composed of s- and p-orbitals. In most metal structures electronic density is almost constant at every place except at the core sites, which is approximate 10 % of the total volume. So, taking the background charge density as constant is satisfactory for our purposes, which is to find the charge distribution and potential at the outside of metal surfaces.

Electronic charge density

We may write the background charge density in the simplest form as

$$n_+(x) = n \text{ if } x < 0 \quad (2.24)$$

and since background charge density is a function of only x , we expect that $n(x)$ only depends on x with the boundary conditions

$$n(x) = \begin{cases} n & \text{if } x \rightarrow -\infty \\ 0 & \text{if } x \rightarrow \infty \end{cases} \quad (2.25)$$

where $n(x)$ also satisfies the condition that total charge should be zero for a neutral crystal. The charge distribution makes no abrupt changes, but spreads out into vacuum. Outside of surfaces, it goes exponentially to zero, whereas it is oscillatory inside the bulk, reaching equilibrium value. These are the Friedel oscillations.

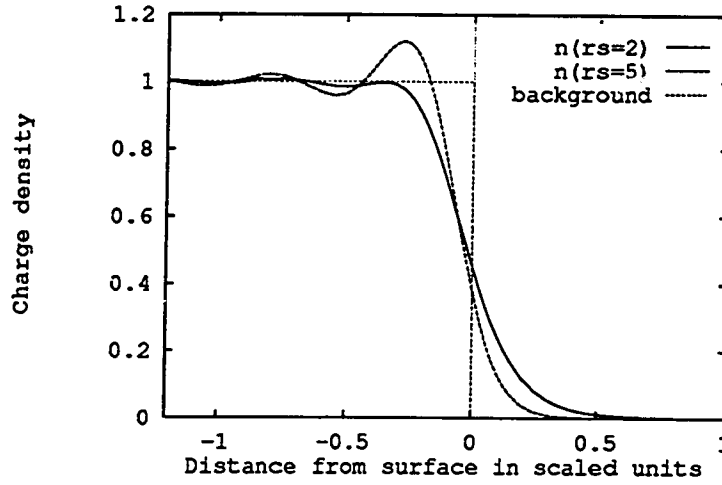


Figure 2.1: Charge density in scaled units for background charge density and for electronic charge density for cases r_s is equal 2 and 5

Effective surface potential and relation to image potential

If we integrate equation 2.8 we can get the following result with an arbitrary constant $\Phi(\infty)$.

$$\Phi(x) = -4\pi \int_x^\infty dx' \int_{x'}^\infty dx'' [n(x'') - n_+(x'')] + \Phi(\infty) \quad (2.26)$$

Since charge density $n(x)$ decays exponentially outside the surface, also $\Phi(x)$ decays exponentially towards $\Phi(\infty)$. The spreading out of the electron density means we get $\Phi(\infty) > \Phi(-\infty)$, which leads to an electrostatic potential for the electrons trying to escape from the surface. The barrier can be calculated by integrating the above equation

$$\Delta\Phi = \Phi(\infty) - \Phi(-\infty) = 4\pi \int_{-\infty}^\infty x[n(x) - n_+(x)]dx \quad (2.27)$$

Note that this $\Delta\Phi$ is the same one as defined in Eq. 2.23, since the mean interior potential $\bar{\phi}$ in the present case is just equal to $\Phi(-\infty)$.

There is also another contribution to the potential energy of the electrons. This is the exchange-correlation energy. In the metal interior each electron lowers its energy by pushing other electrons away to form an exchange correlation hole. This effect also contributes to the effective potential. Since the gradients of $n(\vec{r})$ vanish in the interior of bulk, the effective potential takes a very simple analytical form inside the bulk.

If the electron is far away from the surface, the Coulomb forces are relatively weak and cannot push other electrons inside the bulk. Thus the chance having one electron close to the first one is very small. It has been shown by Rudnick [14] that in this limit, the interaction between the electron and the gas approaches the image potential. The effective potential is thus given by

$$v_{eff}[n; x] \approx \Phi(\infty) - (1/4x) \quad (2.28)$$

at intermediate distances from the surface, both exchange-correlation and electrostatic interactions contribute to the effective potential. A linear response or a weighted density approach can be used to describe the potential in this region.

2.2 Theoretical description of the interaction between atom and surfaces

A detailed derivation of a force formula describing the physisorption interaction between an atom and metal surfaces was performed by Zaremba and Kohn [15]. It was shown that the interaction potential can be written as a sum of two types of

potentials, a van der Waals potential and a repulsive potential.

$$V(z) = V_R(z) + V_{VW}(z) \quad (2.29)$$

This approach will be used for calculation of the trajectories of atoms near surfaces. The repulsive part is due to scattering of the individual Bloch electrons against the incoming atom.

$$V_R(z) = \sum_k \delta\epsilon_k(z) \quad (2.30)$$

where $\delta\epsilon_k(z)$ are band energy shifts caused by scattering of the band electrons from the adsorbate atoms.

The van der Waals term arises from the polarization interaction with the surface. At large distances from the surface, the van der Waals potential can be written as [15]

$$V_{VW}(z) = \frac{C_{VW}}{(z - Z_{VW})^3} + O(z - Z_{VW})^5 \quad (2.31)$$

C_{VW} and Z_{VW} depend on the dielectric properties of the metal and polarizability of the atom .

A more detailed study of the van der Waals and repulsive potential was performed by Nordlander and Harris [16]. These authors derived an expression for the Van der Waals potential valid at small separations from metal surfaces.

$$V_{VW}(z) = -\frac{C_{VW}}{(z - Z_{VW})^3} f(k_c(z - Z_{VW})) \quad (2.32)$$

where

$$f(x) = 1 - [2x(1 + x) + 1]\exp(-2x) \quad (2.33)$$

These expressions for the van der Waals potential behave regularly at $z = Z_{VW}$, and approach for the finite value $V_{VW}^0 = 1.33C_{VW}k_c^3$. In the limit $k_c \gg 1$, the

Van der Waals potential defined in 2.32 approaches its asymptotic value which is defined in equation 2.31. k_c is the cut-off wavelength and its value is approximately (size of atom)⁻¹

The next step is the approximation of the repulsive potential. It can be given in a very simple form to within a few percent error as

$$V_{Rz} = V_0 e^{-\alpha z} \quad (2.34)$$

This formula overestimates the exact repulsive potential at very small distances. This does not affect the present trajectory calculations, since the velocities will be low.

The forces can be obtained directly from these expressions (Appendix A). From the definition of force, $F = -\nabla V_{pot}$. The repulsive force takes the form

$$F_{rep} = -\nabla(V_0 e^{-\alpha z}) = V_0 \alpha e^{-\alpha z} \quad (2.35)$$

and the van Waals force takes the form

$$F_{VW} = C_{VW} \left(-\frac{3}{(z - Z_{VW})^4} f(k_c(z - Z_{VW})) + \frac{1}{(z - Z_{VW})^3} \frac{df(k_c(z - Z_{VW}))}{dz} \right) \quad (2.36)$$

In the case of ions outside the surface, the effective potential of the surface should be included in the force equation. This effective potential was defined in the previous section for the jellium model.

In the figure 2.2 we plot the approximate potentials for the atom surface interactions. The figure shows all the potentials which affect the atom including the image potential, which requires the incoming atom to be an ion. In this figure two total potential lines are drawn, one is the sum of the repulsive and the Van der Waals

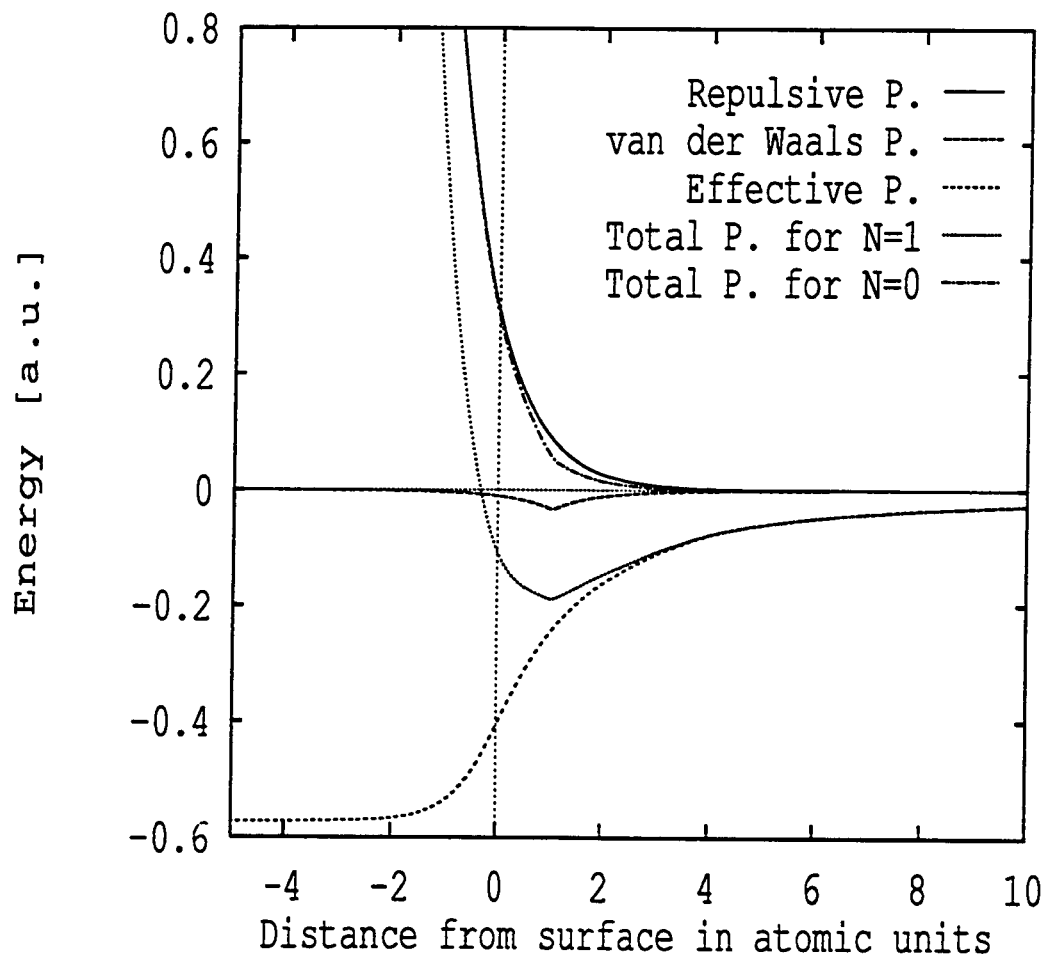


Figure 2.2: Image, repulsive, van der Waals and total potential for a clean Aluminium surface. The potentials are given in a.u. The dotted line is the total potential, the dashed line is the surface and image potential, the long-dashed lines is the Van der Waals potential and the solid line is the repulsive potential. The dot-dashed line is the potential seen by a neutral atom, sum of the Van der Waals and the repulsive part. (The minimum of this potential occurs at the distance of 5-7 atomic units and cannot be seen in this graph)

potentials, whereas the other one includes the image potentials which are applicable to the ions or charged particles near surfaces.

Chapter 3

Tunneling rates near surfaces

Charge transfer process at surfaces are usually described using dynamical theories based on the Anderson Hamiltonian. The energy shifts and the lifetimes of the atomic levels are crucial parameters in these models. The final state of an atom can be strongly influenced by the transitions that occur near surfaces, where the atomic state becomes resonant with the Fermi energy of the metal. These kind of transitions can also happen at large distances from the surface. It is therefore important to know the energy shifts and the lifetimes of the levels for a broad range of atom surface separations.

The theoretical calculations of the energy shifts and the lifetimes of the excited atomic orbitals are difficult. The density functional theories are very difficult to use for excited state calculations and LDA is valid only for small adsorbate-surface separations. Moreover, the excited states of the atoms near surfaces become resonances, which are not square integrable. The standard techniques used for the bound states are therefore not applicable in this case.

Numerous attempts have been made to calculate atomic level shifts and lifetimes near surfaces with idealized surface functions or with perturbation theory [17][18]. None of these techniques have employed an accurate surface potential nor included the hybridization of the adsorbate levels in the presence of the surface potential.

These effects turn out to be essential for obtaining the correct widths of the excited states.

If we add impurities to the surface, the accurate treatment of the surface potentials and the impurity induced potentials are much more important for the calculation of the lifetimes. The fields generated by the impurities are non-isotropic and they can effect the hybridization of the adsorbate levels at larger distances compared to the clean surfaces. Previous calculations which depend on the perturbation techniques and idealized potentials cannot represent these interactions accurately.

Tully and Nordlander [19] developed a method for the calculation of these energy shifts and lifetimes with the Complex Scaling method. In this section we review the Complex Scaling technique. We will show how this method has been used to calculate the lifetimes and the energy shifts of the atomic levels. We will show the limitations of the present approach and suggest an alternative solution for the problem. In the last section the results from both approaches are compared and new results are given, which can not be obtained with the present technique.

3.1 Calculation of Resonance States of Atoms near Metal Surfaces in the presence of Impurities

There are two main steps in calculating the tunneling rates. The first step is to calculate the electron potential in the surface region. The second step is to solve the Hamiltonian imposing resonant boundary conditions.

3.1.1 Calculation of the potential

Although the basic features of the surface potential can be understood from a simple image model, such an approximation will be a crude model for our purposes. Especially the lifetimes of the atomic levels are influenced from the details of the surface potential. The reason for the broadening of the levels is the existence of the continuum of the metal states, into and out of which the electrons can tunnel. The jellium model is used to describe the surface. The impurity-induced potential also has large effects on the tunneling rates and the shifts of the atomic levels. The presence of the impurity atoms on the surface creates anisotropic fields around them which effect the hybridization of the atomic levels.

The electron potential at a given position outside the surface is the superposition of different components. The first component is the bare surface potential. The next component is the proton-induced image potential. The third component is the impurity induced potential on the surface if there are impurities on the surface. If we denote electron coordinates with (ρ, z) in cylindrical coordinates, the position of the impurity with Z_I and the position of the proton with Z , then we get the total potential as

$$V^{(eff)} = V_0^s(z) + \Delta V_A^s(\rho, z; Z) + \Delta V_I^s(\rho, z; Z_I) + \Delta V_{AI}(r, Z, R_I) \quad (3.1)$$

The last term $\Delta V_{AI}(r, Z, R_I)$ describes the change in the surface potential due to interaction between the Hydrogen atom and the impurity. This term will be neglected due to large hydrogen-surface separations. And estimate of the influence of this term on the resonant energies can be found by comparing the transfer matrix element $|\langle \Psi_H | 1/r | \Psi_I \rangle|^2 / (\epsilon_H - \epsilon_I)$ with the width of the hydrogen resonances. It is shown

that for the relevant H and impurity states, $\Delta V_{AI}(r, Z, R_I)$ term can be neglected at the distances larger than 10 a.u. [8] .

Metal surface potential without impurity

There are different methods for the calculation of the surface potential $V_0^s(z)$ for a clean metal surface. We use the density functional electron-surface potential computed by Ossicini [20] for the potential at small distances from the surface. We invoke the weighted density approximation [21] to get a smooth transition from the bulk potential to the image like behavior at large distances as described in the first chapter. This is particularly important since at large distances from the surface the broadenings of the levels depends on the image effects. This many body approach describes the potential in the bulk and the potential at the small surface separations. At large distances from surface the asymptotic limit of the image potential is valid and our potential approach to the theoretical image potential $V_o \rightarrow -1/4(z - z_{im})$, where z_{im} is the image plane defined as the first moment of charge distribution induced by an external electric field.

Proton induced potential

This potential term has two parts. The first one is the electron proton interaction. The second one is the electron and proton-image interaction. The electron proton interaction is easy to calculate for the H case. It is simply $-1/r$ for Hydrogen. For any other adsorbate a pseudopotential is used to represent the nucleus and the core electrons.

The interaction between electron and the image of the proton does not follow the simple image potential $1/\sqrt{\rho^2 + (z + Z - 2z_{im})^2}$ close to the surface. The proton induces a negative charge distribution on the surface centered at z_{im} which gives rise to both an image like electrostatic potential and changes the total exchange-correlation potential close to the surface.

For the intermediate distances we use a linear response approach. Since the exchange correlation effects are local, they do not have any influence at the large distances from the surface and electron-proton image interaction approaches its image potential value. Therefore for the small distances from the surface, we use LDA to calculate the effects of the positive ion core to the total potential, since it gives effectively the same results as DF theory.

The charge induced on the surface is contained within a region of thickness Δ centered around z_{im} . Δ and z_{im} depend on the r_s of the metal [22]. The charge distribution can be approximated by a model charge distribution of the form

$$\sigma(\rho', z', Z) = \frac{1}{\sqrt{\Delta}} e^{-\left(\frac{z'}{\Delta}\right)^2} \sigma_{CL}(\rho', Z - z_0) \quad (3.2)$$

where z' is the distance from the image plane, ρ' is the distance from the surface normal and ρ_{CL} is classical charge density for an infinite plane. Using this approximation for the charge distribution induced on the surface we can solve the Poisson's equation and calculate exchange-correlation correction for the potential. The parameters for this potential are taken from Lang and Kohn paper[22].

Impurity induced surface potential

When impurities are chemisorbed on the surface, they can create strong bonds with the surface. These bonds create strong anisotropic fields around the impurity because of the rearrangement of the charge distribution. The impurity potential is effectively screened inside the metal, because of the high electron density at metal surfaces in the range of the chemi-absorption distances. This is an anisotropic effect because the electron density is decreasing exponentially in our uniform background jellium model of the metals as we go towards the vacuum direction. The calculations of the impurity induced potential are non-trivial and are not the subject of this thesis. This potential is used as an input in our program, therefore we are going to discuss it without going into details.

The potentials are calculated self consistently using the local-density approximation and a jellium model for the surface [7]. The calculations of the impurity induced potential are limited to a sphere of radius 6-8 a.u.. The widths of the atomic resonance states are sensitive to the details of the surface potential in a relatively extended region of the space. Therefore this potential should be extrapolated over all space.

The impurity potential inside the surface has electrostatic, exchange and correlations parts. The induced exchange and correlation potential follows the Friedel oscillations around the impurity. At large distances these oscillations are small and therefore their contribution to the total potential can be neglected. The induced electrostatic part of the potential outside the self-consistent calculated sphere should satisfy Poisson's equation.

$$\nabla^2 V(\vec{r}) = 4\pi\rho_s(\vec{r}) \quad (3.3)$$

In the linearized Thomas Fermi approximation [23], the screening charge density for the induced potential can be calculated by the formula

$$\rho_s(\vec{r}) = \frac{1}{4\pi} q_{TF}^2(\vec{r}) \cdot V(\vec{r}) \quad (3.4)$$

where $q_{TF}^2(\vec{r})$ is a function of both local surface charge density and local Fermi energy.

$$q_{TF}^2(\vec{r}) = \frac{6\pi\rho^0(\vec{r})}{\varepsilon_F(\vec{r})} \quad (3.5)$$

Now using the self-consistent calculation as a boundary value at the sphere, we can calculate $V(\vec{r})$ outside the sphere using the relaxation method. (The algorithms are given in Numerical Recipes [24])

3.1.2 Calculation of the shifts of atomic levels near surfaces using complex scaling

When an atom comes close to the surface atomic levels shift and becomes resonant levels. In order to calculate these shifts we have to solve the Schroedinger equation under the resonance boundary conditions, which can be described as

$$\Psi(\vec{r}) \rightarrow \frac{1}{r} e^{ik_R r + k_I r} f(r, \Omega) \quad (3.6)$$

where k_I is positive. The total energy is equal to $\frac{1}{2}(k_R + ik_I)^2$. The real part of the complex energy is the energy of the level and the imaginary part is lifetime or half-width of the resonance. The Schroedinger equation to be solved is quite general and can be written as

$$[-\frac{1}{2}\nabla^2 + V^{eff}(\rho, z; Z)]\Psi = \varepsilon\Psi \quad (3.7)$$

$V^{eff}(\rho, z; Z)$ is the potential seen by the electron, so that in our case it is the sum of all the potentials we defined in the previous section (Eqn. 3.1). It is obvious that these boundary conditions are diverge at infinite distances. This is an expected behavior because total number of particles in the system should be conserved. The time evaluation of the resonance states can be written as

$$|\Psi(r, t)|^2 = e^{-2\epsilon_I t} |\Psi(r, 0)|^2 \quad (3.8)$$

At infinite time the integral of this expression over all space has to be finite. A method for the solution of this Schrodinger equation under resonant boundary conditions is the *complex scaling method*. A review for the complex scaling method was given by Reinhard and Junker [25]. In this method, the radial coordinate in the Hamiltonian 3.7 is scaled with a complex number as

$$r \rightarrow r e^{i\theta} \quad (3.9)$$

Under this scaling our boundary condition becomes

$$\Psi(r) \rightarrow e^{i(k_R \cos \theta + k_I \sin \theta)r + (k_I \cos \theta - k_R \sin \theta)r} \quad (3.10)$$

It can be seen immediately that this wave function goes to zero in the limit where $r \rightarrow \infty$, provided that the condition $\theta_s > \arctan \frac{k_I}{k_R}$ is satisfied. We can thus diagonalize our Hamiltonian using a normalizable basis. The advantage of this method is that it has simpler boundary conditions, however we have to invert and find the eigenvalues of the complex nonhermitian Hamiltonian matrix. In all calculations integrals are taken in two dimensions since we reduce complexity by aligning the impurity and hydrogen atom along the same surface normal. The basis set for hydrogen is primarily

generalized Laguerre polynomials,

$$\Phi(nlm) = e^{-\frac{\lambda r}{2}} r^{l+1} L_n^{2l+2}(\lambda r) Y_{lm}(\Omega) \quad (3.11)$$

where $Y_{lm}(\Omega)$ is a spherical harmonic and L_n^{2l+2} is a generalized Laguerre polynomial. The matrix elements are calculated on a two centered grid using Gauss Quadrature whenever possible for efficient integration.

The accuracy of the calculations can be checked by investigating the dependence of the calculated eigenvalues on the parameter θ_s . For a complete set of basis functions, there should be no θ_s dependence provided $\theta_s > \arctan(k_I/k_R)$. For a limited number of basis functions, this condition can only be satisfied for the clean surfaces. Both the real and the imaginary part of the resonance energies will slightly vary with θ_s in the presence of the impurity induced potential. The eigenvalues will, therefore, form trajectories in complex coordinate space. It has been shown that under certain conditions the complex energies satisfy a generalized variational principle, such that with a limited basis, the resonance energy will be stationary with respect to θ_s , [26]. Thus we are varying θ_s and looking the particular angle which satisfies

$$\frac{\partial}{\partial \theta_s} \epsilon_R = \frac{\partial}{\partial \theta_s} \epsilon_I = 0 \quad (3.12)$$

The complex energy which satisfies the equation 3.12 is the eigenvalue of the Hamiltonian under the resonant boundary conditions.

Limitations of the present approach

The most important limitation of the current approach is the inability to describe impurities with very large electropositivity. As we can see from the figure 3.1, the

Cs-induced potential is much more extended outside the surface and its magnitude is 3-4 times larger than the Na-induced potential. Therefore, it is very difficult to describe the problem with such a small basis set as for the Na-covered surfaces. Calculations using this basis set for hydrogen outside a Cs impurity failed and very slow convergence was obtained for the K impurity. The reason for this is that the H centered basis functions distribute themselves around the impurity rather than around the hydrogen.

Another limitation of the one-center approach is the description of the ground state (1s) of the hydrogen. Since this state is localized very close to the hydrogen center, the basis functions suited for this state can not describe the affects of the impurity on the lifetimes of the ground state.

By significantly extending the number of basis-functions around the H, the results should converge. In this case the extension to off-axis geometries will be impossible and numerical problems arise because of the size of matrices used in the calculations.

By extending the basis set to a two-center basis, it will be shown that the number of the basis-functions can be drastically reduced. This extension will enable both the calculation of the off-axis geometries and the calculation of the lifetimes of the ground states of the adsorbates. It will be also shown that, this extension will increase the accuracy of the previous results and will incorporates the affects of the impurity-induced states on the excited states of the adsorbate.

Our main aim with this project is calculating resonant states of simple molecules like H_2 and O_2 near the surfaces. This approach clearly requires two-center basis-functions.

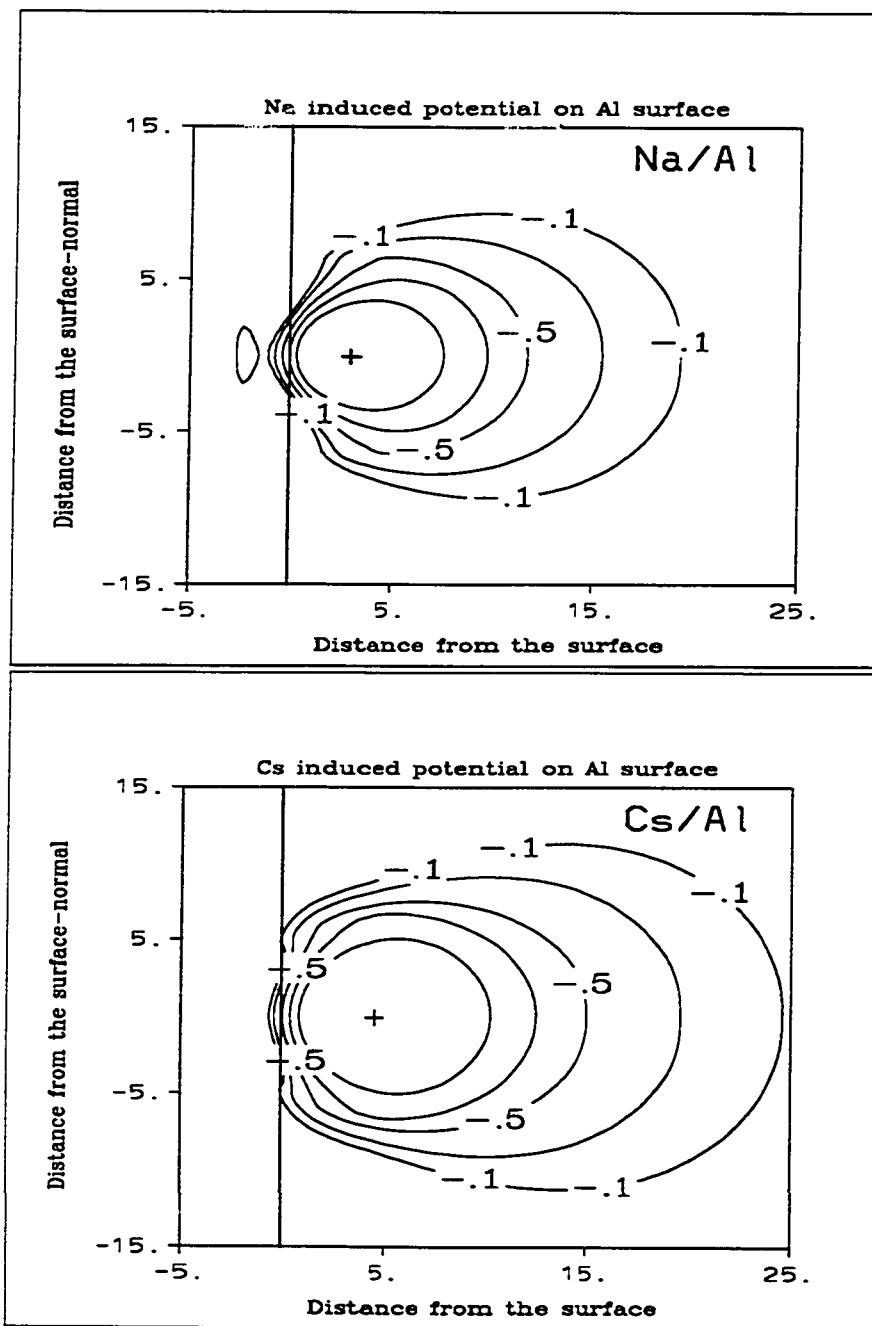


Figure 3.1: Contour plot of the Na and Cs potentials on the Al surface. The contours are at the values -.1, -.3, -.5, -1, -2 eV from outside towards inside. The vertical line is the jellium edge. It can be seen easily that the Cs potential is extended much more compared to the Na potential and its magnitude is larger

3.2 Two-centered basis functions and complex scaling

There are several difficulties involved with introducing a two-center basis. Since the wave functions are not orthonormal, the overlap matrix elements between two centers must be calculated. Another difficulty is that no accurate algorithm for solutions of generalized eigenvalue problems for complex matrices exists. Coordinate transformations are trivial in real coordinates, however after scaling with a complex number, singularities and branch points appear in the region of integration.

The geometry for the present calculations is chosen to be especially simple in order to make use of the symmetry and to reduce the number of dimensions of the problem. The details of the geometry of the problem are given in appendix B with proper coordinate transformations. In this section it will be described how the complex scaling is applied to the second center.

There are different approaches for this problem in the literature, and a general discussion is given by Reinhardt [25]. We implement the method called *Complex Coordinate Born-Oppenheimer Approximation*. In this approach, every radial distance from the Hydrogen center is scaled with a given complex angle θ_S . The subscript S stands for scaling and helps distinguishing the complex scaling angle from the angles used in two or three dimensional coordinate systems.

When the radial distance between the hydrogen center and the impurity center is scaled, a complex distance between two atoms is obtained .

$$\begin{aligned}
 r_I &= \sqrt{d^2(\theta_S) + r^2(\theta_S) - 2d(\theta_S)r(\theta_S) \cos(\theta)} \\
 &= \sqrt{(de^{-i\theta_S})^2 + (re^{-i\theta_S})^2 - 2de^{-i\theta_S}re^{-i\theta_S} \cos(\theta)}
 \end{aligned} \tag{3.13}$$

$$= e^{-i\theta s} \sqrt{d^2 + r^2 - 2dr \cos(\theta)} \quad (3.14)$$

This has two essential consequences. First, since our impurity radial distance is scaled like the counterparts on the hydrogen, they preserve their normality under the complex transformation around the H atom. For this reason, calculation of the kinetic energy elements and overlap matrix elements for the complete set of the wave functions on any center can be done for the real case and later all the results can be scaled. However, the overlap and the kinetic energy matrix elements between the basis-functions around the hydrogen center and around the impurity center are no longer scaled by a simple factor. Therefore, all the kinetic energy and overlap matrix elements together with the potential matrix elements must be calculated for each different scaling angle θ_s , instead of only calculating the potential matrix elements at each θ_s . Furthermore, the radial and the angular integrations can not be separated anymore for the cross matrix elements between different centers. This will increase the computational time approximately by the number of angular points on the mesh.

3.2.1 Geometry of the problem

The system is composed of three components. The impurity, the adsorbate and metal surface. The center of the impurity and the center of the adsorbate are on the same surface normal. This geometry is cylindrically symmetric, since the surface induced potential depends only on the distance from the surface and the impurity and adsorbate centered potentials are cylindrically symmetric. The distance from the center of the impurity to the surface is denoted as Z_I , and the distance of the adsorbate from the surface is Z_H . The position of the electron w.r.t. the impurity

and the adsorbate center are labeled as r_i and r respectively. The integrations are performed around the centers in cylindrical coordinates.

The relevant transformations between the coordinate systems to evaluate wavefunctions are given in appendix B.

3.2.2 Calculation of the matrix elements of the Hamiltonian

First, the calculation of the matrix elements between basis-functions centered on the same center will be explained, then the multi center approach will be discussed. Details of the the derivations are given in the appendix. The matrix element of the Hamiltonian has the form,

$$H_{ij}(\Theta_s) = \int d\vec{r} \Psi_i(\vec{r}) H(re^{i\Theta_s}, \Omega) \Psi_j(\vec{r}) \quad (3.15)$$

If all the terms in the Hamiltonian were analytic functions of the radius r , it is a straight forward procedure to construct the complex Hamiltonian and find its

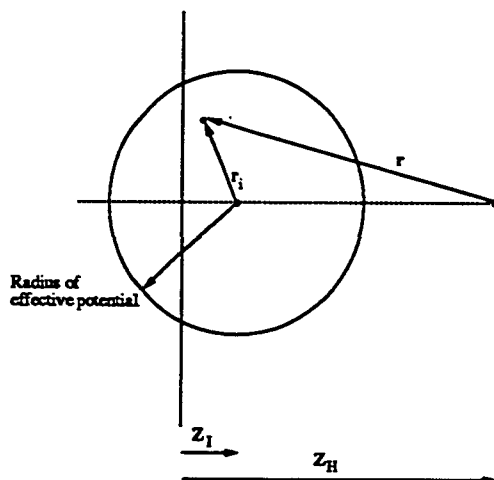


Figure 3.2: Geometry of the problem

eigenvalues. The effective potential on the surface and the impurity-induced potential are only known in numerical form. Therefore a change of variables has to be made in the integration by scaling r as $r \rightarrow re^{-i\Theta_s}$ to get a real Hamiltonian.

$$H_{ij}(\Theta_s) = \int d(\vec{r}_t) \Psi_i(\vec{r}_t) H(r, \Omega) \Psi_j(\vec{r}_t) \quad (3.16)$$

where $\vec{r}_t = (re^{-i\Theta_s}, \Omega)$. \vec{r}_t is used whenever transformation of the position vector is needed and it is written in the vector form.

The expectation value of this real Hamiltonian between complex basis-functions can be evaluated numerically. Since our wavefunctions are analytic, the KE term can be calculated analytically for one-center expansion.

The potential term is the total potential of the electron at any point in space. The integration grid must be chosen so that the strong variation of the potential near the impurity and the hydrogen atoms are accounted for.

The electron-proton interaction has no numerical singularities, because the $1/r$ term is canceled with the volume element $r^2 dr$. The impurity-induced potential is partitioned into two components. The first component is the smoothly varying part of the impurity-induced potential and the other one is the fast varying component. The latter part is confined into a sphere radius r_{cut} . The first part of the impurity-induced potential with the rest of the potentials is defined as $V^{(1)}$. The latter part is labeled as $V^{(2)}$ and integrated on the impurity center, such that the volume element $r^2 dr$ cancels the singular behavior in the second part of the impurity-induced potential. The construction of the matrix elements for these potentials are explained below.

Calculation of $V_{ij}^{(1)}(\Theta)$

This matrix element can be written, after the same coordinate transformation as in 3.16, as an integral over all space of a real potential between the complex wavefunctions.

$$V_{ij}^{(1)}(\Theta) = \int d\vec{r}_i \Psi_i(\vec{r}_i) V(r, \Omega) \Psi_j(\vec{r}_i) \quad (3.17)$$

This integral can be written after rearranging the terms and using the Gauss theorem for the integration in this simple form

$$V_{ij}^{(1)}(\Theta) = e^{-i\Theta} \sum_{k=1}^{Nk} \tilde{\Psi}_i(r_k) \tilde{\Psi}_j(r_k) S_{l_i, l_j}(\frac{r_k}{\lambda_R}) \quad (3.18)$$

where pseudo-basis-functions are defined as

$$\tilde{\Psi}_i(r_k) = C_i(\lambda) \sqrt{\frac{W_k}{\lambda_R}} e^{i \frac{\tan \Theta}{2} r_k} \chi_i(\frac{r_k}{\cos \Theta} e^{-i\Theta}) \quad (3.19)$$

and $S_{l_i, l_j}(\frac{r_k}{\lambda_R})$ is the result of the angular integration for a given radius.

The details of these steps are in appendix D.

Calculation of $V_{ij}^{(2)}(\Theta)$

Here, the calculation of the matrix elements of the Hamiltonian for the $V^{(2)}$ potential will be discussed. Since this potential is centered around the impurity and is very deep, the integrations are performed around the impurity center. This enables us to cancel the large potential at the small radius from the impurity center with the volume element $r^2 dr$, in such a way that the singularities vanish. These calculations are very time consuming and difficult because the integrations can no longer be performed from the center of the basis set. The radius of integration around the impurity center was

chosen such that, at that radius (r_{cut}) the average impurity potential is comparable to the sum of other potentials so that a smooth connection from the potential $V^{(1)}$ to $V^{(2)}$ can be made. The details of the definition of the matrix elements $V_{ij}^{(2)}$ are in the Appendix D and the final result is

$$V_{ij}^{(2)}(\Theta) = e^{-i\Theta} \int_0^{r_{cut}} dr_I \int_{-1}^1 d\xi \bar{\Psi}_i(r_I, \xi_I) V^{(2)}(r_I, \xi_I) \bar{\Psi}_j(r_I, \xi_I) \quad (3.20)$$

where $\bar{\Psi}_i$ are the pseudo-basis-functions.

3.2.3 Addition of the impurity-based basis set

Definition of the basis set

An orthonormal basis set is created around the impurity such that there is no need to take into account the effects of overlap matrix elements except the ones between two different centers. Since they are exponentially proportional to the distance between two centers, they are smaller compared to the diagonal elements. This guarantees us the invertibility of the overlap matrix S with an accuracy of 11-12 digits.

The basis set around the impurity center is defined similarly to the basis set around the hydrogen atom. The only difference between these two basis sets is the parameter λ used in the exponential factor. For the impurity-centered basis functions $\lambda_I \approx 4 - 5$ whereas $\lambda_H \approx 1$ for $n=2$ states.

The basis-functions have the form:

$$\Psi_{I_i} = C e^{-\lambda_I r_I} L_n^{2\ell+2}(\lambda_I r_I) (\lambda_I r_I)^\ell P_{\ell,m}(\cos(\theta)) \quad (3.21)$$

and as a consequence

$$\langle \Psi_{I_i} | \Psi_{I_i} \rangle = 0 \quad (3.22)$$

This type of basis sets, expanded around both impurity and H, create an overlap matrix which has four blocks; the diagonal blocks are unit matrices, and the elements of non-diagonal blocks have a magnitude which is $\ll 1$.

The different matrix elements which are not computed for the one-center calculations are overlap matrix elements for kinetic energy and the total potential. The remaining matrix elements are technically the same as the adsorbate centered matrix elements.

Thus, the required matrix elements are $\langle \Psi_{I_i} | \nabla^2 | \Psi_i \rangle$ and $\langle \Psi_{I_i} | V_{total} | \Psi_i \rangle$

It is clear that, the basis functions are not an orthonormal set of wavefunctions anymore. Therefore finding of the eigenvalues of the total Hamiltonian is not sufficient and the generalized complex eigenvalue systems should be solved. If we begin with the Schroedinger equation 3.7

$$\left[-\frac{1}{2} \nabla^2 + V^{eff}(\rho, z; Z) \right] \Psi = \varepsilon \Psi \quad (3.23)$$

and construct the matrix elements we get

$$\begin{aligned} \langle \Psi_i | H | \Psi_j \rangle &= \langle \Psi_i | \varepsilon_j | \Psi_j \rangle \\ (\langle H \rangle - \langle S \rangle \varepsilon) \Psi &= 0 \\ \det | \langle H \rangle - \langle S \rangle \varepsilon | &= 0 \end{aligned} \quad (3.24)$$

The coefficient of the ε is transferred to the identity matrix by multiplying the equation from the left with S^{-1} , the inverse of the S matrix. Thus the solutions depend on how well the S matrix can be inverted, and also on the sensitivity of the inversion to small changes in the S matrix. If the sensitivity is too large, all the elements have to be calculated on a very fine grid, which is not desired. If we define S^{-1} as the

inverse of the overlap matrix S , we will get

$$\begin{aligned} \det|S_{ij}^{-1}H_{jk} - S_{ij}^{-1}\varepsilon S_{jk}| &= 0 \\ \det|S_{ij}^{-1}H_{jk} - I_{ij}\varepsilon| &= 0 \end{aligned} \quad (3.25)$$

In the next sections, it is shown how to compute the necessary matrix elements under complex scaling.

Calculation of kinetic energy matrix elements

As mentioned earlier, the calculation of matrix elements for the impurity centered wavefunctions are the same as the adsorbate centered ones. The extra kinetic energy elements which are needed are of the form

$$KE_{overlap} = \langle \Psi_{I_i}(r_I, \Omega_I) | \nabla^2(re^{i\theta}, \Omega) | \Psi_i(r, \Omega) \rangle \quad (3.26)$$

where $\Psi_{I_i}(r_I, \Omega_I)$ are basis-functions around the impurity center and, $\Psi_i(r, \Omega)$ are basis-functions around the adsorbate center. The kinetic energy operator is invariant in spatial translation, therefore the same KE matrix elements are obtained between two basis-functions independently from the origin of the coordinate system. If 3.26 is written in its integral representation with real coordinates, it will take the form

$$KE_{overlap} = \int d\vec{r} \Psi_i(r, \Omega) \left(\nabla^2(re^{i\theta}, \Omega) \Psi_{I_i}(r_I, \Omega_I) \right) \quad (3.27)$$

where kinetic energy matrix elements are defined from the adsorbate center and the integral is over all space. In the one-center expansion of the wavefunctions, the complex part can be taken out of the kinetic energy operator outside the integral and the result will be a complex constant premultiplying the real kinetic energy matrix

elements, which are trivial to calculate. Because of the oscillatory behavior of the wavefunctions, it is not possible to do this for the multi-center expansion of the basis and coordinate transformations should be performed to convert the complex kinetic energy operator to a real one. This makes the basis-functions complex, and the real derivatives of the complex variables should be taken, instead of complex derivatives of the real functions. These steps are in appendix D, and the final form of the matrix elements can be written as

$$KE_{overlap} = e^{-3i\theta_s} \int d\vec{r} \Psi_i(re^{-i\theta_s}, \Omega) \left(\nabla^2(r, \Omega) \Psi_{I_i}(r_I e^{-i\theta_s}, \Omega_I) \right) \quad (3.28)$$

Calculation of potential and overlap matrix elements

Potential and overlap matrix elements follow the same procedure as the kinetic energy matrix elements. The same transformations are used to obtain the complex basis-functions and to analytically continue the complex potential to the real axis. The relevant matrix elements are then calculated from the effective potential of the system. The general form of the matrix elements can be written as

$$V_{ij} = \langle \Psi_{I_j} | V_{total} | \Psi_i \rangle \quad (3.29)$$

where $V(\vec{r}, Z, Z_I)$ is given in the equation 3.1

3.3 Results of the two centered complex scaling method

In this section, we will first show that the two-center expansion of the basis-functions is much more accurate and requires much fewer basis-functions to solve the problem.

First the concept of convergence of the results are defined, which will be very helpful in further discussions. There exist two types of convergence. First, the solution obtained with a given basis set converges to a value satisfying the general variational principle defined in equation 3.12. Second those results coming from different basis sets converge to a unique value. This means that adding more basis-functions won't change the results significantly. In this case five percents is an acceptable value, because this has higher accuracy than the methods used to construct the surface and impurity potentials.

In figure 3.3, the basis-functions are expanded only around the hydrogen atom which are converged in the sense that the results satisfy the generalized variational principle. The results are plotted from three different basis sets, the smallest consisting of 100 basis-functions with $l_{max} = 10$, the biggest of 288 basis-functions with $l_{max} = 18$. As seen from the figure, each of the basis set satisfies the variational principle, and the set of 288 basis-functions has a very small deviation when changing the complex scaling angle. None of them approach the same value.

There are two solutions for a better convergence. One is increasing the size of the basis set, and making it more complete. However, this is not possible in a numerical calculation with a total 15 digits of accuracy. The invert a matrix and find its eigenvalues requires approximately N^3 operations, which reduces the significant digits in the final result. Also, using higher numbers of basis functions requires using bigger angular quantum number l and principal quantum number n . This increases the effective range of the basis-functions. Therefore, for an accurate calculation of the proper matrix elements with the existence of the surface and the impurity potential,

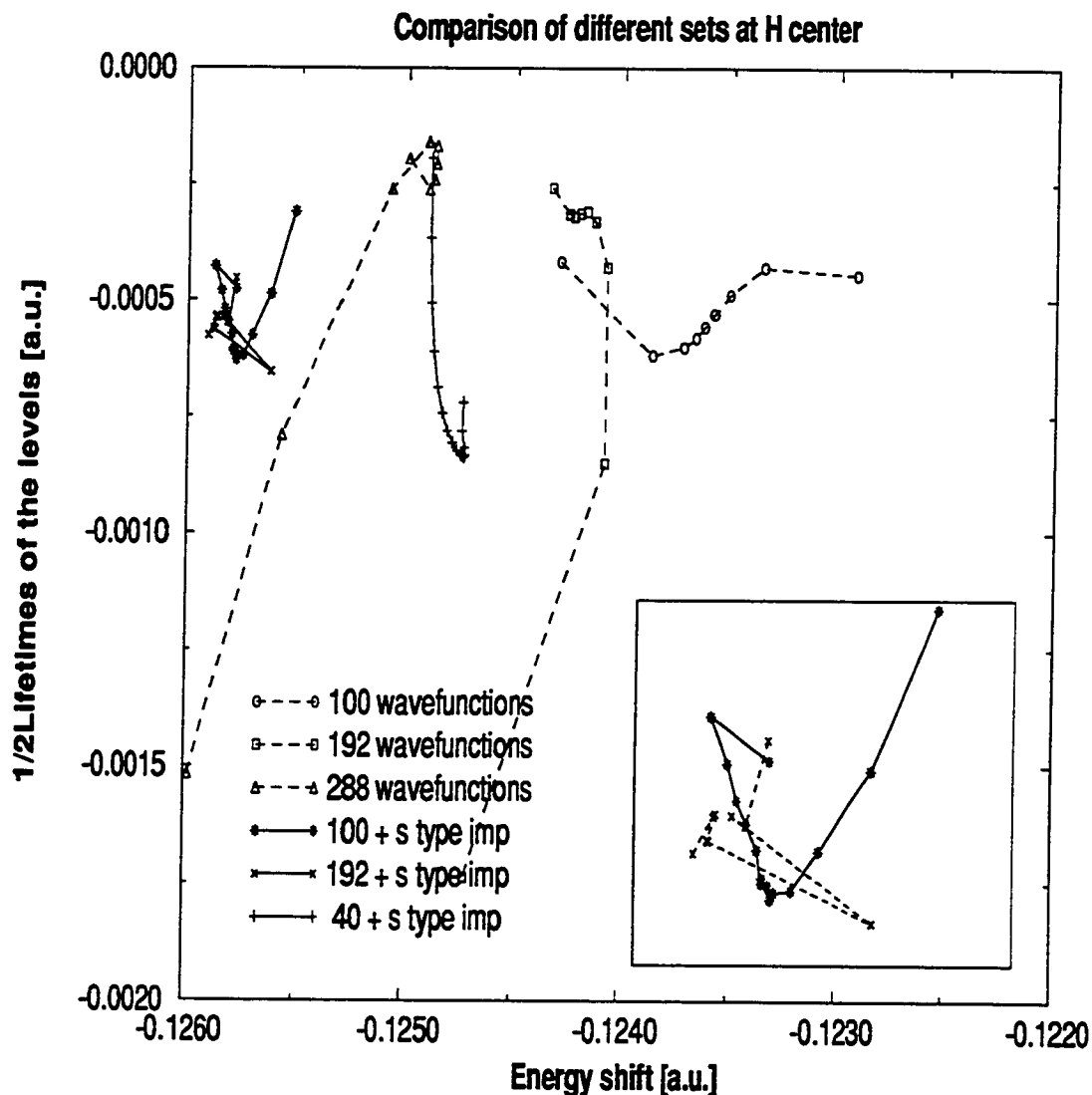


Figure 3.3: The convergence of different basis-function sets at adsorbate center with the existence of s basis-functions on the impurity center. Dashed lines are from the one-center expansion of the basis set (○:100, □:192 and △:288 basis-functions) and the solid lines are from two-center expansion (★:100 H-centered + s-type impurity centered basis-functions, ×:192 H-centered + s-type impurity centered basis-functions and +:40 H-centered + s-type impurity centered basis functions). The dashed lines do not converge to one point. The solid lines converge to the same point for 100 and 192 basis-function sets and give a reasonable result with only 40 basis-functions around the H. The rectangle at the right corner is the zoomed view of the graphs in the left-up corner.

we need a much higher number of grid points, and all of these extra calculations reduce the significant digits in the Hamiltonian matrix even further before we begin to find the eigenvalues of the Hamiltonian.

The second solution is to add some basis-functions where they are needed most. A much better convergence is obtained in this case, due to the fact that, the representation of the impurity-induced potential with the impurity-centered basis-functions is more accurate compared to the adsorbate based basis functions. Figure 3.3 shows the results of addition of the basis-functions of s-symmetry around the impurity . It is clear that, all the basis sets approach to the same value regardless of the size of the basis-function set around the Hydrogen center. Therefore, we can conclude that addition of the basis-functions on the impurity center makes the basis-sets much more complete than the basis sets we can get from one-center expansion of the basis sets.

Adding p-states to the impurity basis change the results again significantly. The reason for this is that the two main potentials which affect the lifetimes of the Hydrogen states are the surface potential on a clean surface and surface potential and impurity potential on the impurity covered surface. It can be seen from the figure 3.1 that the surface potential around the impurity center, which is 3-4 a.u. at a distance from the surface, is composed mainly of s- and p_z -states, which are $l = 1$ and $m = 0$ states (Figure 3.4). In addition to this, the impurity potential has also the p_z dependence. Because of the screening of the bulk electrons, the impurity potential is a one sided potential expanded away from the surface. This type of potential can be expressed by hybridization of the s- and p-orbitals. Therefore the information

in p-states is important and at least s- and p-type basis-functions are needed in the impurity-centered basis set.

Since tunneling between the surface and the adsorbate is due to the overlap between the extensions of the surface states perpendicular to the surface and adsorbate levels as discussed in the previous chapter, the correct representation of these states is important. The addition of only s-type basis functions on the impurity covers most of the singularity of the potential, but the long range effects are described mainly by $l = 1$ states.

The effects of the addition of p-states on the impurity center is shown in the figure 3.5. The real parts of the complex energy increase. The addition of the $l = 1$ states also increases the imaginary parts of the complex energy. Since the resonance band widths are proportional to the imaginary part of the energy, this results in an increase in the tunneling rates between these levels and the surface.

All the graphs show the calculations for the adsorbate distance of 16 a.u. . This is the distance where the best convergence for the one-centered expansion of the basis-functions is obtained. At distances 20 a.u. and larger it is difficult to span the whole space with a one-center approximation and at closer distances the overlap of the impurity and surface potential with the proton potential is too large, so that it is difficult to find a good convergence. Another point is that, in the cases like Cs, the basis-functions try to span Cs states instead of the aimed adsorbate states.

3.3.1 Results for the excited states of H on Na/Al

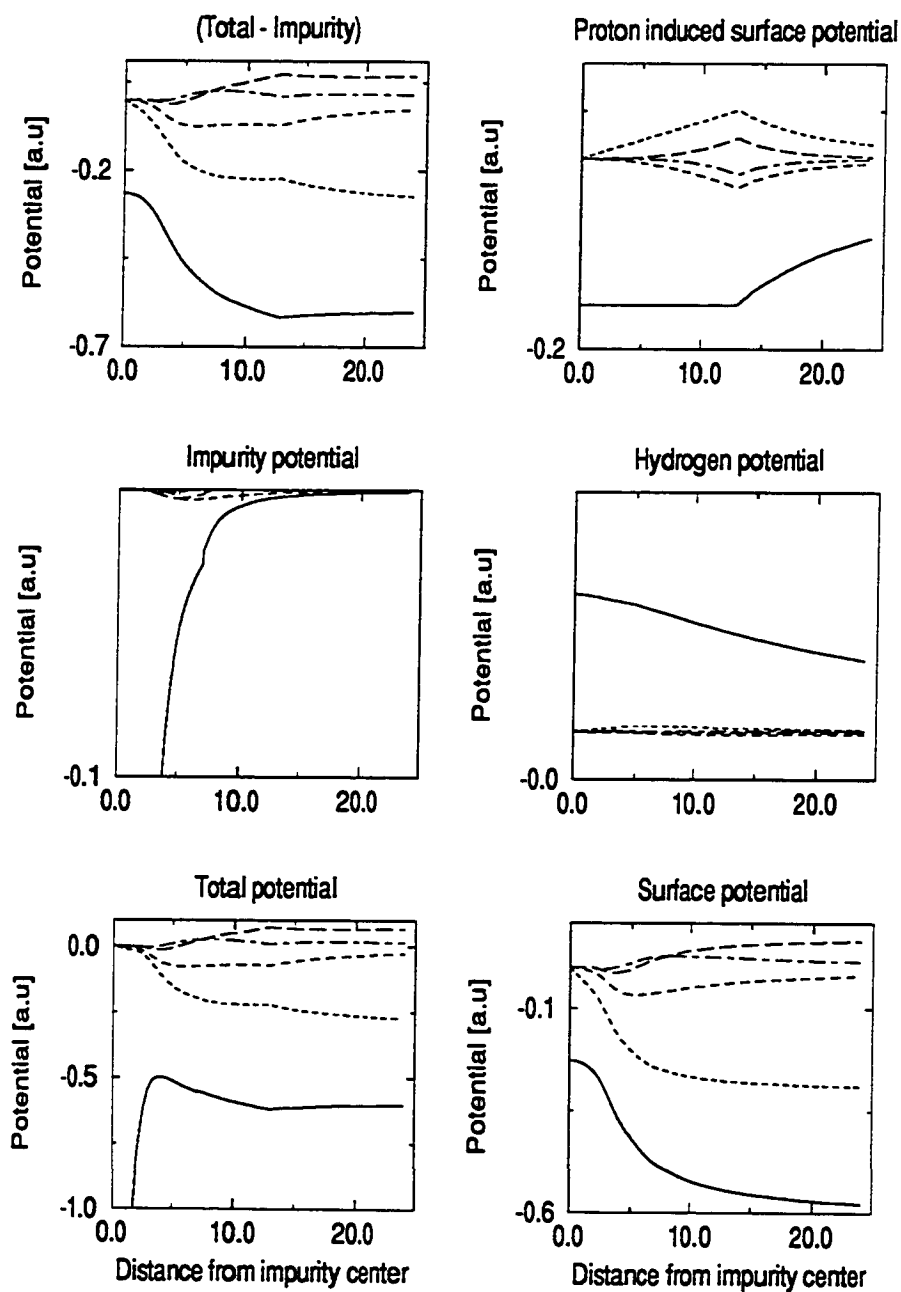


Figure 3.4: Angular distribution of the potential as seen from the impurity center. The solid lines are $l=0$ components of the potential, dotted lines are $l=1$ components, dashed lines are $l=2$ components, long dashed lines are $l=3$ components, dashed-dotted lines are $l=4$ components.

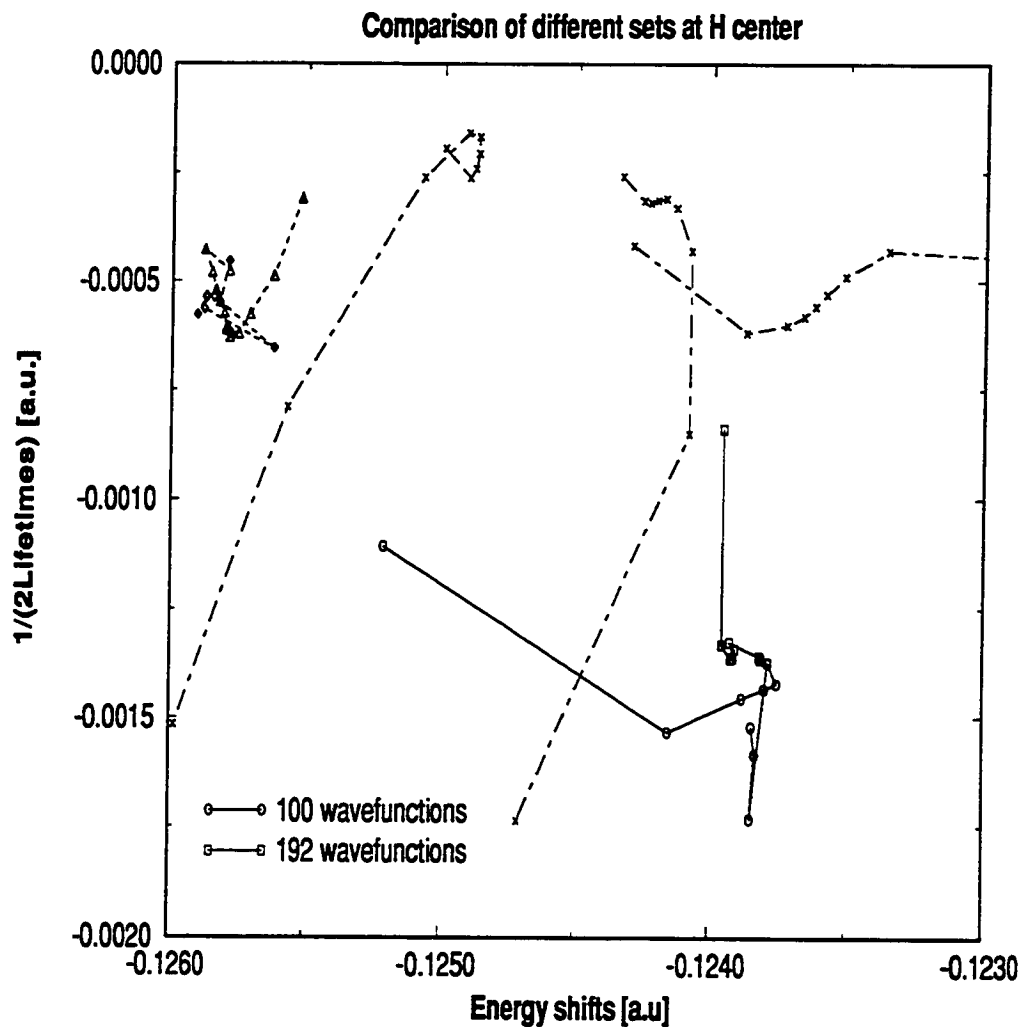


Figure 3.5: The convergence of different basis-function sets at adsorbate center is shown with the existence of s- and p-type basis-functions on the impurity center. The solid lines are for these states (○:100 H-centered basis-functions + s- and p-type basis functions on impurity center, □:192 H-centered basis-functions + s- and p-type basis functions on impurity center), the dashed lines in the upper left corner have only s-type basis-functions and the dot-dashed lines are for the one-center expansion as explained in the figure 3.3.

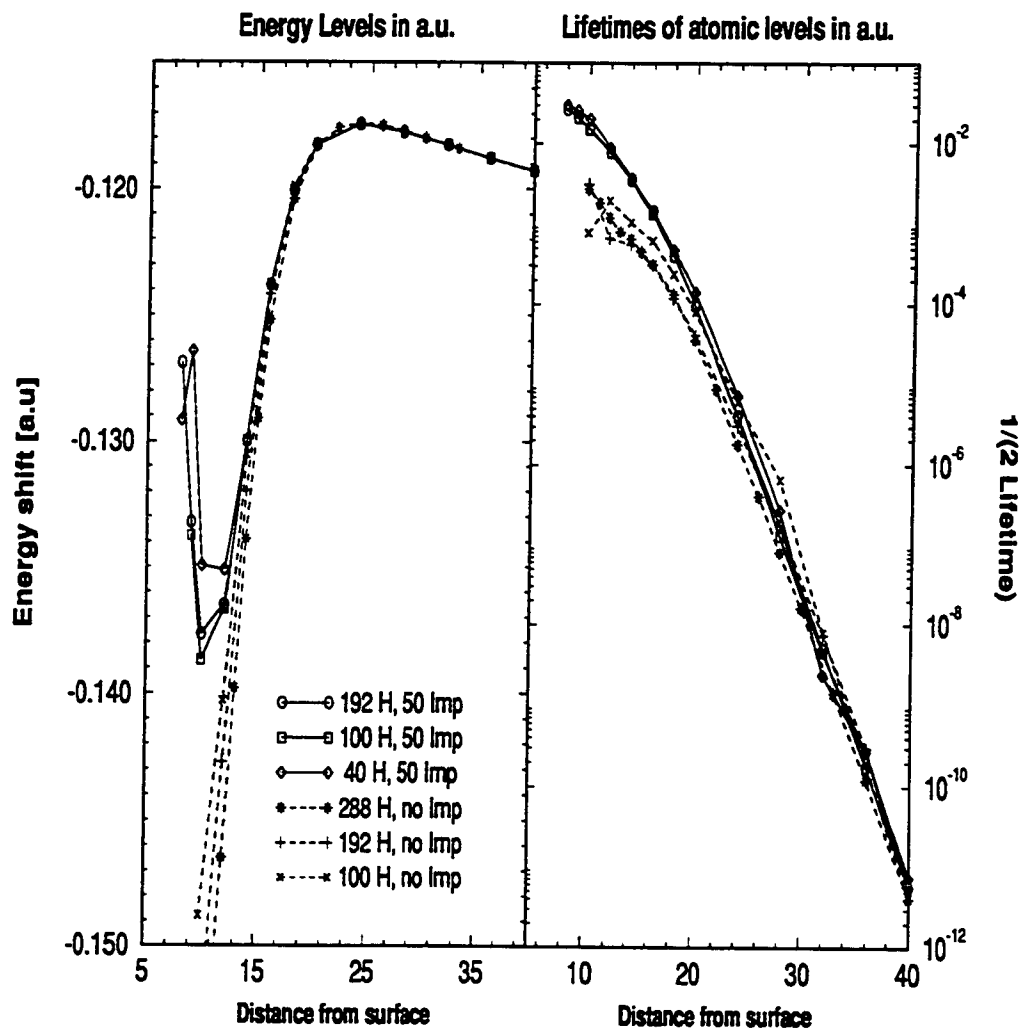


Figure 3.6: The left graph shows energy levels for the $n=2$ and $m=0$ states (oriented towards the surface) and the right one shows the lifetimes for the same states calculated with different basis-sets. Dashed lines are for the one center expansion and solid lines are for the two-center expansion of the basis sets. The basis functions on the impurity center have $l = 0, 1, 2$ and 3 states. The solid lines show the effects of Na levels on the Hydrogen levels as the upshift of the energy levels.

In figure 3.6, the atomic levels and lifetimes are compared for H on the Na covered Al surface from the calculations with one one- and two-centered expansion of the basis-sets. The one-center expansion of the basis-functions has been made with three different sets, namely 100, 192 and 288 basis-functions around the adsorbate. Calculations using less than 100 basis functions do not converge. Even in the 100 basis-function set, the lifetimes are oscillating around the lifetimes of the 288 basis-function set. The energy level of the states can be determined with smaller basis sets if the adsorbate is far from the surface, because the H levels are not coupled with any of the surface or impurity states. The energy levels begin to deviate from each other for different sets when the adsorbate is brought closer to the surface. This shows that in the presence of the impurities, a complete basis set cannot be formed by expanding the basis-functions only around the adsorbate center.

When the above results are compared with the two-center basis, it can be seen that even 40 wavefunctions will produce a fairly good approximation both for the lifetimes and energy levels close to the surface. The energy levels in all cases come out the same if the adsorbates are outside 16 or 18 a.u. from the surface. Initially, they follow the same trend and later the two center results begin to curve up and the levels begin to shift up instead of down. This can be explained from the fact that the missing impurity states in the one-center expansion pushes the levels up again because of the exclusion principle. This physical effect was not described accurately in the previous approach.

The lifetime graphs from both methods look very similar. The only difference is the shifts in the graphs, which actually corresponds to a factor of two or three times

difference in the lifetimes, which can not be seen easily from the graph because of the logarithmic scale. At closer distances, this ratio increases further, up-to a factor of 10 or more. The lifetimes in general are increased by a factor of two to three, which is understandable because the overlap elements are expressed in a more accurate way. The reason that they do not have so much effect on the energy levels is that for the energy shifts due to overlap matrix elements are first order perturbation to the actual value whereas for the lifetime contributions from the overlap matrix elements are directly proportional to the results.

3.3.2 Results for the ground state(1s) of H on Na/Al

The shift and broadening of 1s-states could not be calculated using a one-center expansion of the basis-functions. Hydrogen 1s states on clean surfaces could be calculated and it is shown that it follows the lifetimes of the $n=2$ $m=0$ state which is oriented away from the surface on the clean metal surfaces. With the present technique, it is possible to calculate the lifetimes of the 1s state of H on impurity covered metal surfaces.

Figure 3.7 shows the shifts of the 1s level of the H atom in vicinity of the Na covered aluminum surface. The real parts of the complex energy, which are energy level shifts of the ground state of H, shifts down as we approach to the surface. The results are obtained for the H-surface separations up to 8 a.u. . Since Na is at 3 a.u. from the surface, we are 5 atomic units away from the Na^+ center.

The lifetimes have the same order of magnitude as the lifetimes of the $n=2$ states which are oriented away from the surface. This is similar to what was found previously

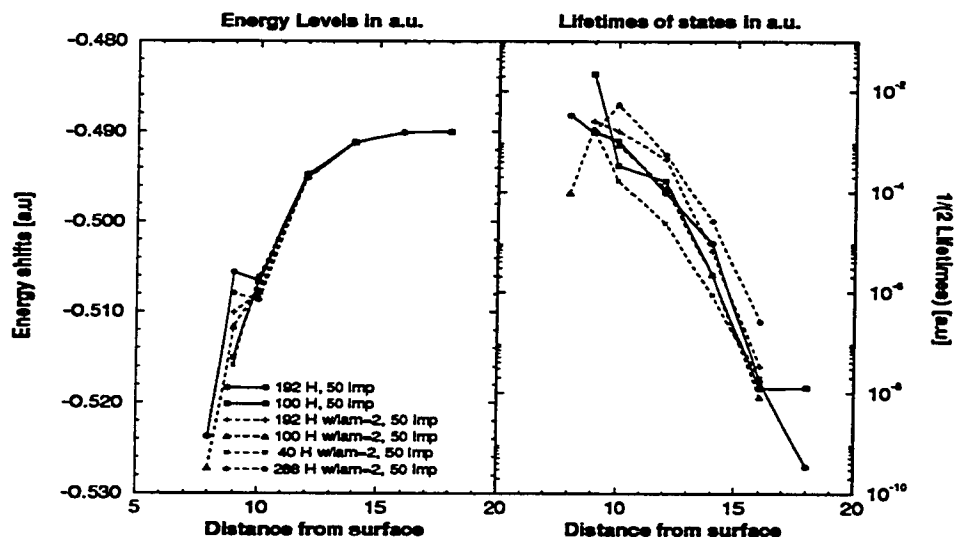


Figure 3.7: H/Na/Al results for $n=1$ state. The left graph shows the energy level shifts for Hydrogen $1s$ state in the vicinity of Na covered Al surface. The right graph shows the lifetimes of the $1s$ state on the H. Solid lines are calculations for $\lambda_H = 2$ and the dashed lines are for $\lambda_H = 1$ (Calculated at the same time with $n=2$ states)

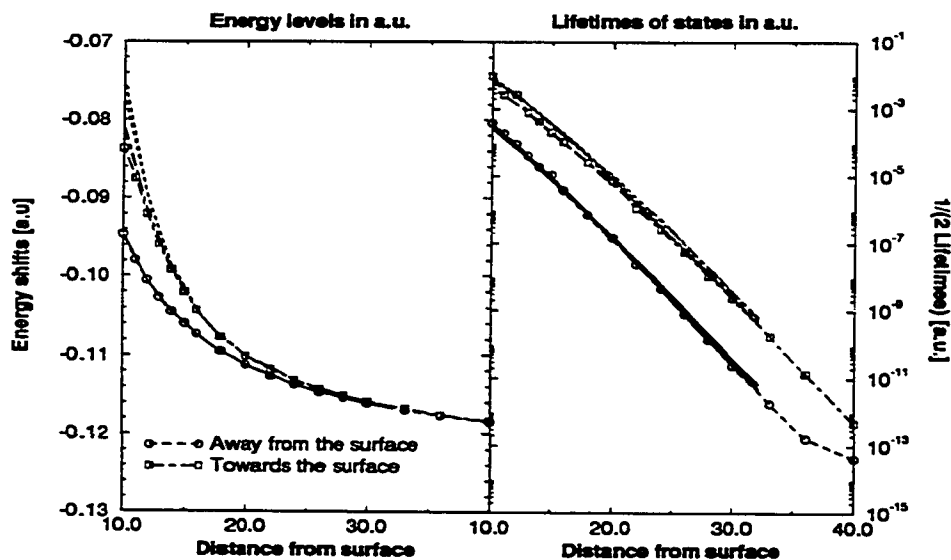


Figure 3.8: The energy shifts and lifetimes of the Hydrogen $n=2$ $m=0$ states near the Cl covered Al surface. The lines with \circ are oriented away from the surface and the lines with \square are oriented towards the surface. Each group contains 7 different basis set but individual lines can not be distinguished from each other.

for H on clean surfaces. The dotted lines on the figure correspond to the values obtained from the calculations with a basis set having the correct exponential factor for the 1s state, $\lambda = 2$. The data for the solid lines comes from the calculations for $n=2$ state.

3.3.3 Results for Cl states

The results for Cl-covered surface are very different from those of alkali covered surfaces. The Cl potential is repulsive and does not support any bound states. Therefore the lifetimes are much longer than the alkali states.

In figure 3.8 it can be seen that the lifetimes have exponential form and the energy shifts are in the opposite direction. Therefore, when the adsorbate comes towards the surface, the levels shift up and the ionization energies will decrease. Although it is difficult to distinguish the various plots, the graph contains the results from both one- and two-center expansion of the basis-functions for different basis sets. The results are independent of the basis sets and the one- or the two-center expansion of the basis functions have very little effect on the results. Only at very small atom-surface separations, a small difference can be detected. (The one which is oriented away from the surface has almost the same results for all different basis sets.)

These results are expected and confirm the accuracy of both approaches for the cases where there is no strong potential depth near the surface. The new and the old approach begin to deviate from each other at small adsorbate-surface separations, but for the charge transfer purposes both methods gave the same results. Another important point is that, at small distances, it will become more difficult to find the

eigenvalues as a function of the scaling angle, for the approach where we used one-center based expansion of the basis-functions. The deviation of the eigenvalues are, with respect to scaling angle, much smaller in the two-center expansion of the basis-functions.

3.3.4 Results for Cs states

Results for the $n=2$ states of the H near the Cs-covered aluminium surface is given in figure 3.9.

The solid lines are taken from the calculations with only adsorbate centered basis sets. The state which is oriented towards the surface is affected from the Cs impurity and is difficult to calculate. For distances less than 14, we cannot calculate the energy shift of this state and the lifetime curve on the right shows a broken curve shape.

The dashed lines are taken from the calculations with a two-center basis set. The basis set around the impurity contains $l = 0, 1, 2$ and 3 states each having Laguerre polynomials of order 20.

The state which is oriented away from the surface is easily described using either one-center or two-center expansion. The results for the shifts in the energy levels agree with each other. The lifetimes almost follow the same trend in both cases, but the curves for the lifetimes of these states begin to deviate at close atom-surface separations.

The second state is oriented towards the surface. The results for the energy shifts are the same at the adsorbate-surface separations, which are larger than 18-19 a.u. . For closer separations different results are obtained. To explain these results, another

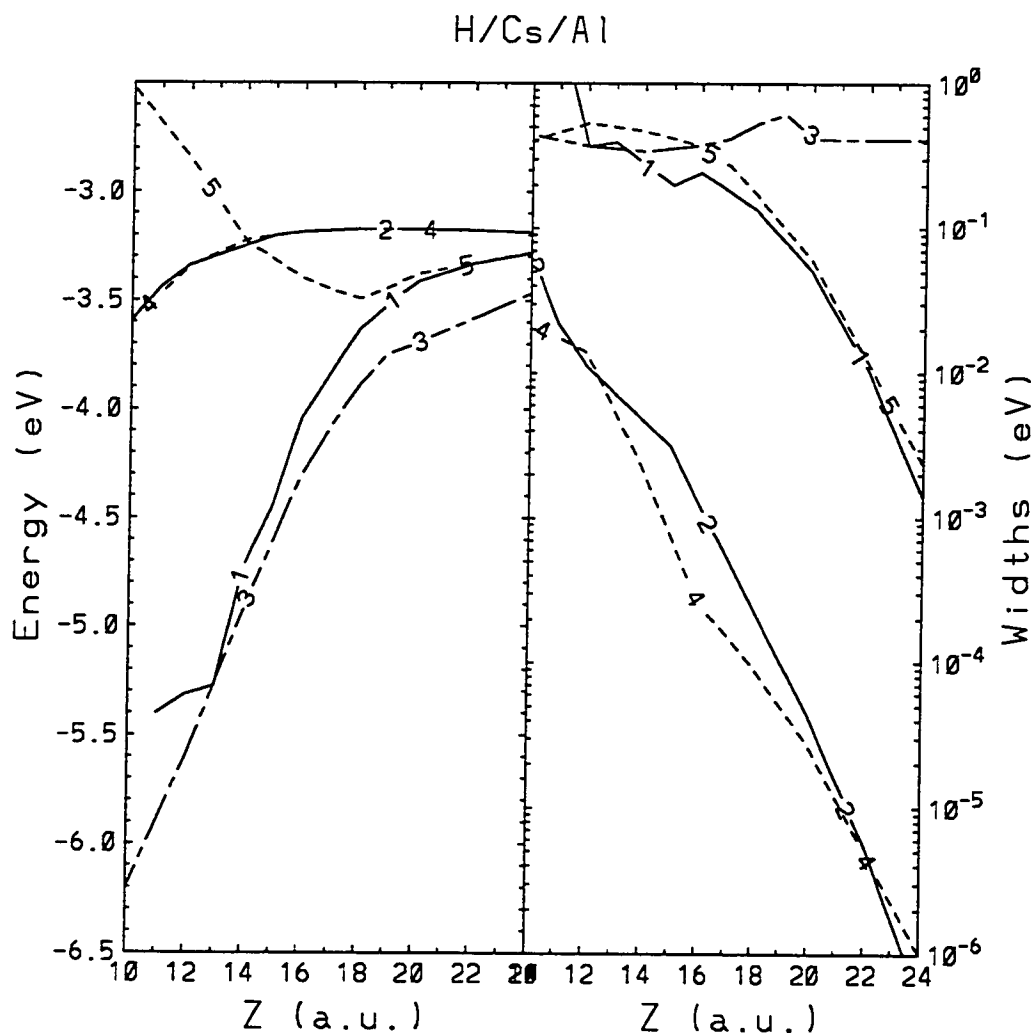


Figure 3.9: The energy shifts and lifetimes of the Hydrogen $n=2$ $m=0$ states near the Cs covered Al surface. The solid lines are from one center expansion of the basis functions, dashed lines are from 2 center expansion of the basis functions. The long dashed curve is probably a Cs state or another Cs-H hybrid state, which interacts with one of the $n=2$, $m=1$ states of the H. (Lines labeled as 2 and 4 are the states oriented away from the surface. Lines labeled 3 and 5 are oriented towards the surface, 5 is two-center expansion and 3 is one-center expansion of the basis set. Line number 4 is a Cs state).

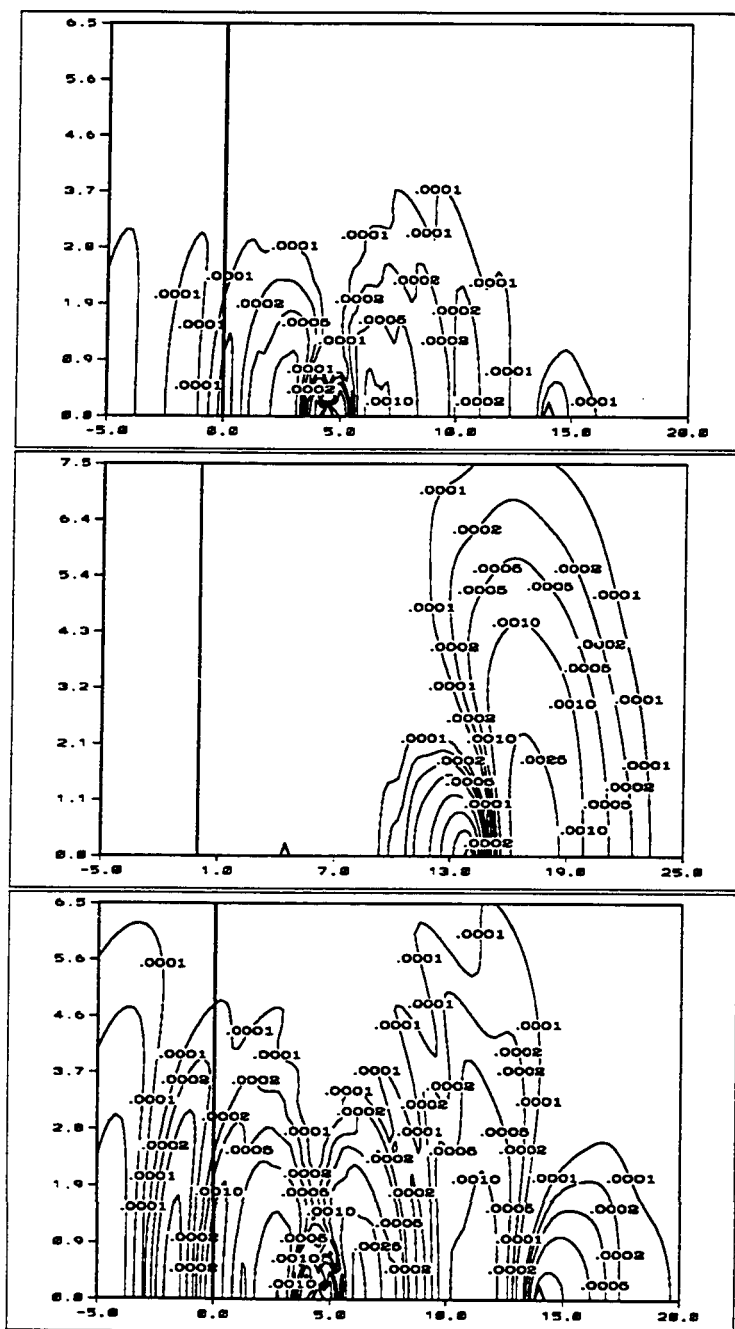


Figure 3.10: The probability distributions of the $n=2$ levels of H on Cs/Al are plotted. The top one is the most electro-negative state and the bottom one is the least electro-negative. The horizontal axis is the distance from the surface and the vertical axis is the distance from the surface normal. The contour lines show the probability distribution in cylindrical coordinates.

state is drawn in the figure. This dot-dashed line corresponds most probably to a Cs-induced state, which was poorly described using one-center basis expansion. These curves are the best representation of the eigenvalues calculated at different adsorbate-surface separations.

To make this point clearer, we plot the probability of the electron for these three states in figure 3.10. In this figure, atom-surface separation is 14a.u. Only the upper ρ -half-plane is plotted. The first figure shows the position probability of the electron for the most electronegative level. The second figure shows the same probability distributions for the intermediate eigenvalue, and it is clear that it is the hybridized $n=2$ state that is oriented away from the surface. The third graph shows the least electronegative state.

The task remaining is to determine which of the figures corresponds to the H state and which to Cs state. The first figure is much more localized around the Cs atom, whereas the third figure is localized around the H and is extended into the surface region. Therefore we conclude that the deepest lying state is not the $n=2$ state of the H, which is oriented towards the surface. In making this decision, the plots of these three eigenstates at the distances 20,18,17,16,14,13,12,10 were used, but only one of them is given here as an example.

When the atom approaches the surface, the two $n=2$ states of H levels cross each other. The lifetimes of the two states are exponentially decreasing far outside the metal surface. However, the lifetimes of the state which is oriented towards the surface do not have a simple exponential decay at the separations between 10-18a.u..

The results for the lifetimes from one-center expansion of the basis shows a broken line behavior, which is not a natural behavior for a physical system.

All these evidences show that, when we are dealing with strong electro-positive impurities on the surface, we have to be careful and use all the potentials which can be calculated with various techniques instead of idealizing or neglecting them.

3.4 Discussion of the results

In previous sections, the results for different impurities were given and they were compared to the results from the old method.

For electronegative impurities, which do not have bound states for an electron, one-center expansion of the basis functions are sufficient to determine the lifetimes and the energy shifts of the adsorbate levels.

Addition of electro-positive impurities to the surface results in strong hybridization between the adsorbate levels and impurity or surface levels. For weakly electro-positive systems, we can perform our calculations with a one-center based approach and obtain very close results to the ones from the two-center based approach, for adsorbate-surface separations larger than 12.a.u. Inside this region, the shifts can be affected by the presence of the impurity levels. In these cases, using the new method utilizes a much smaller basis set, and calculations for different geometries other than the one used here can be performed. These off-axis geometries are important in the sense that in the experiments, most of the flight time for the ions passes at off-axis geometries.

For strong electro-positive impurities, we have shown that the results can change drastically with the addition of the impurity-based basis set. Without these support bases, the eigenvalues are not stationary and very slow convergence is obtained at the atom-surface separations between 12-18a.u.. Therefore we strongly recommend using two-center approach at close surface-atom separations and/or in the presence of the strong electro-negative impurities, like Cs and K.

Chapter 4

Dynamics of Charge Transfer

When an atom is sent towards the surface, due to the shifts of the atomic levels, the atom has a probability of gaining or loosing an electron when it comes back from the surface. The probability of the charge transfer in an atom-surface collision depends both on the energy shift and broadening of the atomic levels and on the trajectory of the atom with respect to the surface.

A common approximation when calculating the charge transfer probabilities is the method called *Trajectory Approximation* or TA. In this method the trajectory of the atom is prescribed and not influenced by any charge-transfer events along the trajectory.

A dynamical theory for charge transfer was first developed using time-dependent Anderson model by Blandin. However, these treatments neglected the spin effects and the effects of the intra-atomic Coulomb interactions.

Recently, another method was suggested for the description of the charge transfer process between metal surfaces and atomic levels, which can be single or multi-leveled. Using Kadanoff-Baym formalism with Coleman's slave boson method, the time-dependent populations of the atomic levels can be calculated [8]. It was shown that for low velocities and finite temperatures the population of the atomic states

can be described by using simple master equations with rates equal to the tunneling rates of the electrons between the atomic levels and the surface.

In the following sections, we will investigate the accuracy of the TA. Two different methods will be considered. In the *Semi Classical Approximation* (SCA), the population of the atomic levels will be determined by integrating the master equation along the trajectory. The atomic potentials depend on the charge state of the atom, which can be fractional. In the *Monte Carlo* based approach only the transfer of a whole electron is allowed and atomic potentials also depend on the charge state of the atom.

4.1 Dynamics of the charge transfer in Atom surface collisions in classical treatment

Dynamics of charge transfer can be examined by integrating two coupled differential equations of the charge transfer rate and the force equation for the atom moving toward the metal surface.

When going beyond the trajectory approximation, the velocity is not taken as constant. The force on the particle, as a function of time, strongly depends on its position and charge. There is a big difference in forces applied to a neutral or charged ion because of the image force, particularly at close distances. The charge transfer rate at any moment depends on the charge of the incoming or outgoing atom, on the width of the band (lifetimes of the states), which determines the probability of charge tunneling process, and on the Fermi level of the surface.

We can write our coupled equations in the simplest form as

$$m \frac{d^2 z}{dt^2} = F_{rep}(z) + F_{VW}(z) + F_{eff}(z, N(t)) \quad (4.1)$$

$$\frac{dN(t)}{dt} = \Gamma(z)(1 - N(t))f(\epsilon_a(z)) - \Gamma(z)N(t)(1 - f(\epsilon_a(z))) \quad (4.2)$$

Here $N(t)$ is the charge on the atom, f is the Fermi-Dirac distribution and z is the distance from the surface.

There are three different terms in the force equation. The origin of these terms was explained in the previous chapters. The image force depends on the charge of the atom. This is one of the main reasons for atom trapping in atom surface collisions.

The second equation, (Eqn. 4.2) describes the electron tunneling process between the metal levels and the atomic level. This is the so called *master equation* of the charge transfer process [8]. The equation consists of two parts. The first part represents charge transfer from the surface to the atom and the second one represents charge transfer from atom to the surface.

Gamma is the probability for the charge transfer rate and was calculated in the previous chapter and in article [27] for various surface-atom pairs. The calculated lifetimes (the imaginary part of the complex energy) of the atomic levels are the half widths of the broadenings of the levels. Therefore, the correct treatment, especially outside the impurity covered metal surfaces, requires the use of these accurate values.

If we examine the master equation more closely, some simple limits can be observed. If the atom has a unit charge, there can not be a charge transfer toward the atom. Hence in our discussions only one unit of charge can be gained or lost. The Fermi-Dirac distribution dictates that charge transfer can be accomplished only when the Fermi level of the surface is higher than the electronic levels of the atom to which

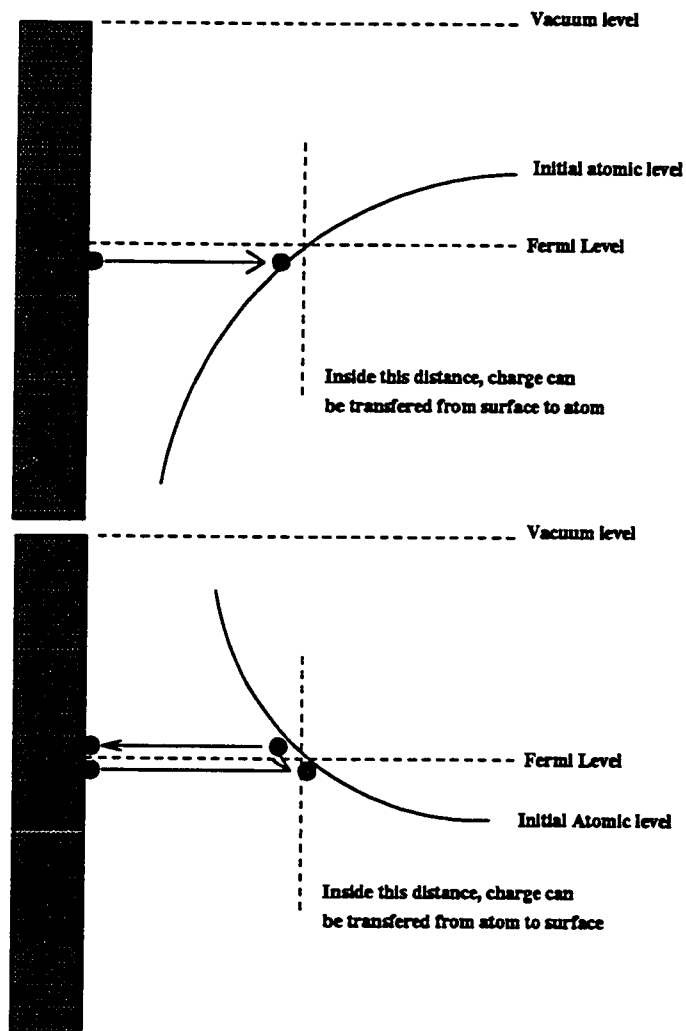


Figure 4.1: Charge transfer from the metal surface to the atom. The top figure shows the charge transfer process for the affinity levels and the bottom figure shows the charge transfer process for the ionization levels.

charge transfer will occur (Fig 4.1). The second term is the charge transfer from the atom to the surface. The condition which is necessary for this process is that there must be a charge on the atom which can be transferred, and there must be a hole in the Fermi level of the surface at the energy level of the atom. That means the atomic level should be at a higher potential than the Fermi level of the surface.

The other variables of the set of equations 4.2 and 4.1 are Fermi-Dirac distribution functions of the surface and the coefficients for the force terms, which describe different materials. The Fermi-Dirac function depends both on the work-function of the metal surface and on the temperature. The coefficients for the force terms are chosen such that the results are applicable to a large class of H-metal scattering cases. These coefficients depend on the properties of the surface material.

In the program, the Fermi level of the metals changes such that it covers the energy range which is below and above the initial atomic level. This approach allows us a qualitative investigation of the charge transfer rates for different kinds of processes, which includes different incoming atoms or molecules having different atomic energy levels. This approach also allows the description of impurity effects on clean surfaces. The charge transfer process depends entirely on the difference between the Fermi level of the metal and the atomic level of the incoming adsorbate; therefore keeping one fixed and changing the other one satisfies our goal. The results of the programs can be interpreted as having different particles coming towards the surface or scattering the same particle against surfaces with different work-functions.

Two different types of atomic levels will be investigated. Neutral levels shift upwards, as shown in figure 4.1b and the affinity levels shift downwards, as shown

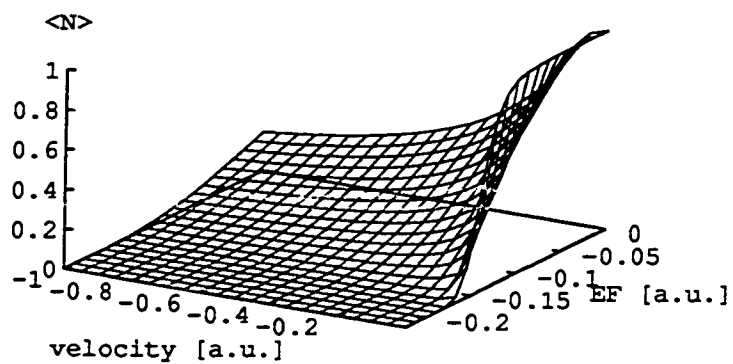


Figure 4.2: Charge transfer probabilities for the ionization levels.

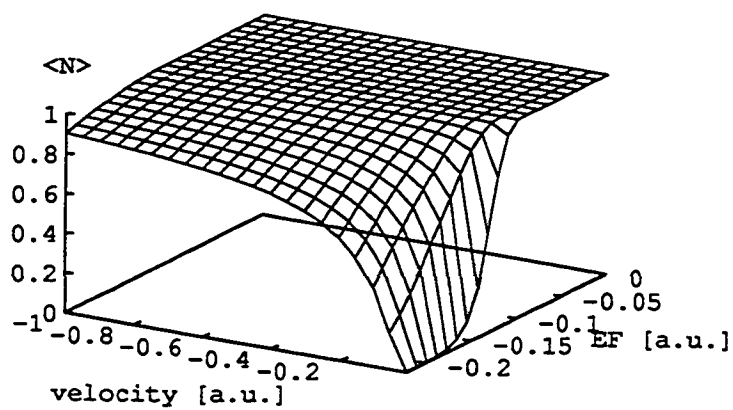


Figure 4.3: Charge transfer probabilities for the affinity levels.

in figure 4.1a. The cases of most interest are the Fermi level crossing of the atomic levels. The shift of the atomic levels near surfaces are treated in general, as if they are shifting up or down, whether they are crossing Fermi levels or not.

The affinity levels are examined in figure 4.3. In this figure, the z-axis shows the total probability for the charge transfer. The x-axis shows the initial velocity of the atom and the y-axis shows the Fermi level of the surface. The initial atomic level is 0.11 a.u. . The shifts of the affinity levels near clean metals are downwards.

If the atomic levels shift down and the initial atomic levels are below the Fermi level, we usually have a complete charge transfer. In this process, the electrons can always tunnel towards the atomic levels but not back towards the surface, since the empty surface levels into which electrons can tunnel are above the Fermi level of the surface. This process is shown in the graph with the flat surface at $N=1$ between the Fermi levels 0 and .11 a.u.

If the atomic levels shift down and the initial atomic levels are higher than the Fermi-level, there are two possibilities. In the first case, the levels will not shift down enough so they do not cross the Fermi level, and therefore no charge transfer is expected toward the atom. In the other case, the atomic levels shift down, such that they go below Fermi level as they approach the surface. In the latter case, we have a charge transfer toward the atom when the atom is inside the distance of the crossing of the Fermi-level and atomic level. In the return path the charge is transferred back to the surface when the atomic levels shift up again. The details of this process and the percentage of atoms carrying a charge out depend heavily on the velocity, tunneling rates, and surface and atomic levels. If the atom is moving slowly, there is enough

time for the transfer of the charge back to the surface and thus we see neutral atoms coming from the surface. For the faster particles this time is relatively short, and negative ions are seen coming from the surface.

The ionization levels are examined in the figure 4.2. In the figure the z -axis shows the total probability for the charge transfer. The x -axis shows the velocity change and the y -axis shows the Fermi level of the surface. The initial atomic level is 0.2 a.u.. The shifts of the ionization levels near a clean metal are upwards.

If the atomic levels shift up and the initial atomic levels are higher than the Fermi level, the atom cannot receive an electron from the surface. If it comes with an electron there is a big probability that it is going to loose its charge to the surface. This region is the flat part of the surface with a Fermi level greater than 0.2 a.u.

If the atomic levels shift up and the initial levels are below the Fermi level, the atom has a tendency to receive a charge at larger distances from the surface. But since this process can happen only outside of the crossing distance of the atomic level and the Fermi level, the probability of the charge transfer depends on the broadening of the levels and on the speed of the electron. If the atom turns before reaching the crossing, there is a small probability of charge transfer. If the particle goes beyond the crossing point it looses all memory of its initial state. The total probability depends on the return leg of the trajectory after the crossing point. In the figure this region is described with a Fermi level less than 0.2 a.u. . For fast moving particles, the time that the particle spends near the crossing distance is much smaller; therefore the probability for the charge transfer is small. As the velocity decreases, the chance of the charge transfer increases. The final electronic state of the atom also depends on

the Fermi level of the surface. As the Fermi level increases (becomes more negative), the crossing distance of the Fermi level and atomic level moves further away from the surface. Since the tunneling rates drop exponentially with increasing distance from surfaces, the probability of the charge transfer decreases as expected. This is easily seen in the figure.

4.2 Dynamics of the charge transfer in atom surface collisions in the Quantum Mechanical picture

The main drawback of the SCA approach is that fractional charges are allowed on the atom. We therefore modify our approach to allow only integer numbers of electron transfers between the atom and the surface.

In order to accomplish this, Monte Carlo simulations were used in which the incoming atom travels from one grid point to the other and the charge transfer probability is calculated between two grid points. When the atom reaches the next grid point (which can be achieved by one or more Runge-Kutta steps), the charge transfer probability is compared to a random number, normalized for the interval [0-1]. This determines the transfer of the charge from the surface to the atom or the other way around. In the limit where the size of the grid separation is decreased to zero, the exact Quantum Mechanical description is obtained. The charge is transferred according to the tunneling properties and at any time the charge on the atom is 0 or a positive integer.

This approach gives results very similar to those obtained by the SCA for velocities greater than 0.01 a.u.. For smaller velocities, different results are seen. The parame-

ters of these calculations do not represent any particular experiment. All parameters, including the coefficients for the force and potential equations, can be varied. The velocity of the atom can be described as slow or fast w.r.t the potentials used. A particle is referred as slow if its kinetic energy is comparable to the image potential where the charge transfer occurs. The reason is that a neutral particle does not feel the image force until it loses its electron when its ionization level passes the Fermi level of the surface, or when it gains an electron when its affinity level passes the Fermi level. If a sudden change of the potential affects the total energy of the incoming atom sufficiently, the total energy becomes negative, and the atom cannot escape from the surface and begins to oscillate back and forth with a decreasing energy until it stops at the middle of the potential well. The reason for the energy loss is in elastic events such as electron-hole pair interaction or multi-phonon process.

This effect is not significant in the SCA, because of the existence of the fractional charges. Thus the atom does not feel a sudden change in potential when it loses or gains a charge. In both approaches, the atom has the same total energy when it is at the closest distance from the surface. In the SCA, it gains charge slowly, such that the potential seen by the atom changes at the same time. As soon as a small charge is transferred to the atom, the atom has a different total energy than the Quantum Mechanical case, where the potential changes suddenly. This smooth variation allows the atom to escape from the surface.

Table 4.1 shows the charge transfer rates for the ionization level of the H atom. SCA is the Semi Classical treatment and MC 1000 is the Monte Carlo simulation with 1000 trajectories. Both cases, where the particle comes with a H atom or with a H^+

Velocity	In. N	SCA	MC 1000	MC 25000
0.1	0	0.048638	0.056056	0.049962
	1	0.04897	0.05905906	0.048242
0.01	0	0.385279	0.37337	0.3859(1/0)
	1	0.45165	0.48748	0.455494(13/2)
0.006	0	0.5453	0.5637(23/11)	0.5629832(527/178)
	1	0.7255	0.84845(157/62)	0.849763(4243/1567)
0.003	0	0.75846	0.80132(166/93)	0.79855(3931/2199)
	1	Stick	0.9805(508/382)	0.9704(12721/7248)

Table 4.1: The comparison of the charge transfer for SCA and MC simulations for 100K

Velocity	In. N	SCA	MC 1000	MC 25000
0.1	0	0.0488774	0.058058	0.05028201
	1	0.04921026	0.05805806	0.04724189
0.01	0	0.385348	0.380380	0.38773(1/0)
	1	0.451304	0.442442	0.447965(15/6)
0.006	0	0.5440524	0.5715726(14/7)	0.5667339(568/199)
	1	0.7222765	0.859743(162/65)	0.869204(4443/1642)
0.003	0	0.7546057	0.7738854(145/57)	0.7908991(3914/1824)
	1	Stick	0.9736457(506/316)	0.97635(12703/7127)

Table 4.2: The comparison of the charge transfer for SCA and MC simulations for 300K

ion, are examined. For the H ion N is zero, which is equivalent to empty ionization levels. The numbers inside parenthesis correspond to the total number of particles which oscillate and escape or stick to the surface respectively. The initial KE of the H atom is approximately $0.55H(\text{a.u.})$. The calculations are done at 100K.

If we look to the velocities of 0.006 and 0.003 a.u. which are comparable to the image potential around that region, quite different results were obtained for SCA and MC. If we neutral particles as neutral to the surface (in this case $N=1$), the difference in the final charge is quite large. The force on a neutral particle is very small and therefore does not affect the velocity of the atom significantly. If the atom comes with a KE such that our total energy is positive even when we include the image potential, it does not stick to the surface. In the MC simulations we see that almost $1/20$ of the incoming particles stick to the surface. The average charge transfer for the escaping trajectories is bigger for MC.

Another important case is that when the incoming particle is neutral and the KE is almost half of the image potential. In the SCA, the particle cannot escape from the surface, whereas in the MC simulations only $2/5$ of the incoming particles stick to the surface and the rest escape.

Table 4.2 shows the same calculations done for 300K. There is no significant change in the final charge transfer rate or in the comparison between SCA and the MC simulations.

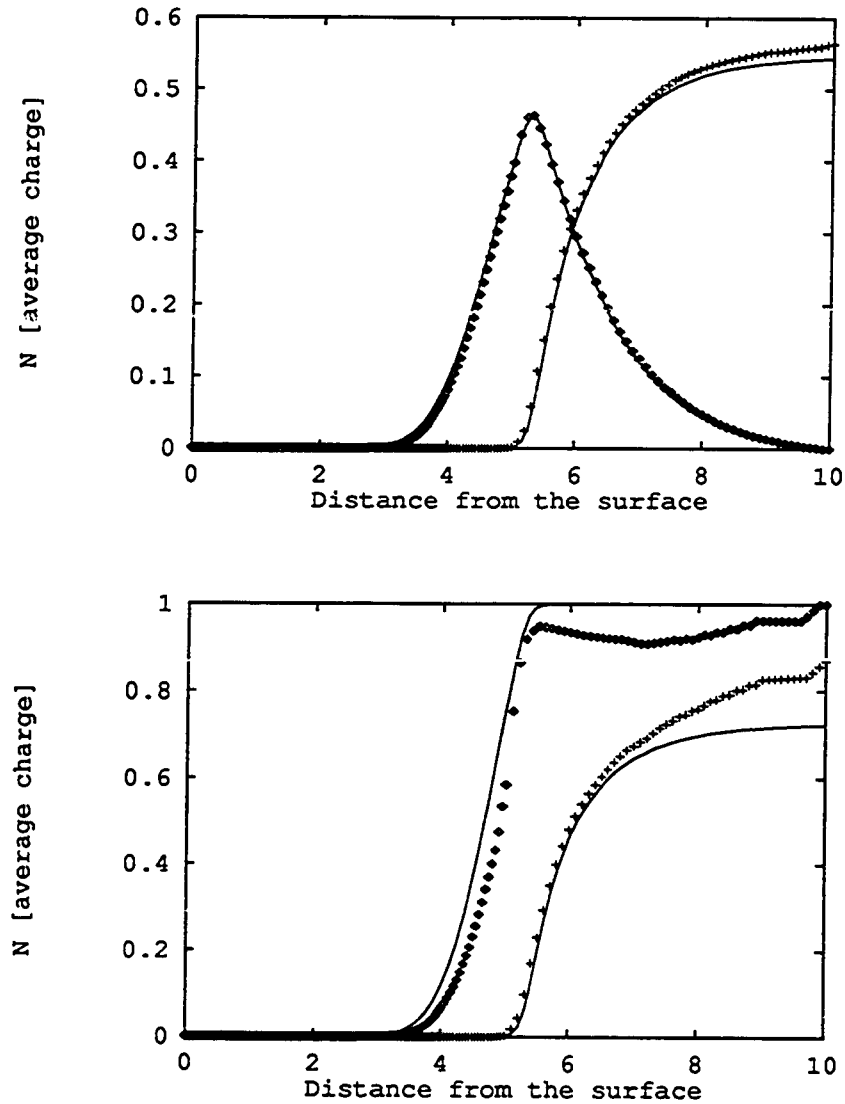


Figure 4.4: The comparison for charge transfer characteristics of SCA and MC simulations for the ionization levels. The top graph is the simulation where the incoming particle is an ion. (Ionization level is empty). The bottom graph shows the same for the case where the incoming particle is a neutral one. Solid lines refer to the SCA. The circles refer to for MC simulations with 1000 trajectories, the triangles are for MC with 25000 trajectories.

Appendix A

Derivation of force equations from potentials

$$F_{VW} = -\nabla \left(\frac{-C_{VW}}{(z - Z_{VW})^3} f(k_c(z - Z_{VW})) \right) \quad (\text{A.1})$$

$$F_{VW} = C_{VW} \left(-\frac{3}{(z - Z_{VW})^4} f(k_c(z - Z_{VW})) + \frac{1}{(z - Z_{VW})^3} \frac{f(k_c(z - Z_{VW}))}{dz} \right) \quad (\text{A.2})$$

where

$$\begin{aligned} f(x) &= 1 - [2x(1+x) + 1]e^{-2x} \\ \frac{df}{dx} &= -[2(1+x) + 2x]e^{-2x} - [1 + 2x(1+x)](-2)e^{-2x} \\ &= -[2 + 4x]e^{-2x} + [4x + 4x^2 + 2]e^{-2x} \\ &= [4x + 4x^2 + 2 - 2 - 4x]e^{-2x} \\ &= 4x^2 e^{-2x} \end{aligned} \quad (\text{A.3})$$

and

$$\frac{df(k_c(z - Z_{VW}))}{dz} = \frac{dx}{dz} \frac{df}{dx} = k_c 4x^2 e^{-2x} \quad (\text{A.4})$$

But as we can easily see, there are singular points in the above equation at $z = Z_{VW}$. If we expand above equation around $z - Z_{VW}$, we get the following expansion.

$$V(y) = \frac{-C_{VW}}{(y/k)^3} [1 - [2y(1+y) + 1]e^{-2y}]$$

$$\begin{aligned}
&= \frac{-C_{VW}}{(y/k)^3} [1 - [2y(1+y) + 1][1 - 2y + 2y^2 - 8y^3/6]] \\
&= \frac{-C_{VW}}{(y/k)^3} [\frac{4}{3} - 2y + \frac{8}{5}y^2 + \dots] \\
&= -C_{VW}k_c^3 (\frac{4}{3} - 2y + \frac{8}{5}y^2)
\end{aligned} \tag{A.5}$$

If y is small($z \rightarrow Z_{VW}$), our potential goes to

$$V_{VW} = -\frac{4}{3}C_{VW}k_c^3 \tag{A.6}$$

and if we substitute y back into the equation and take the derivative we find the force equation in small y ($z \rightarrow Z_{VW}$) limit

$$\begin{aligned}
V_{VW} &= -C_{VW}k_c^3 (\frac{4}{3} - 2k_c(z - Z_{VW})) \\
-\frac{dV_{VW}}{dz} &= -C_{VW}k_c^4 2 \frac{d(z - Z_{VW})}{dz} \\
F_{VW} &= -2C_{VW}k_c^4
\end{aligned} \tag{A.7}$$

Appendix B

Geometry of the problem

In this appendix, the relation between two coordinate systems centered around the impurity and adsorbate is given. Both coordinate systems are cylindrically symmetric.

Derivation of the expressions for $r(r_i, \theta_i)$ and $\theta(r_i, \theta_i)$

$$r(r_i, \theta_i) = \sqrt{(Z_H - Z_I + r_i \cos \theta_i)^2 + r_i^2 \sin^2 \theta_i} \quad (\text{B.1})$$

$$\theta(r_i, \theta_i) = \arctan \frac{r_i \sin \theta_i}{Z_H - Z_I + r_i \cos \theta_i} \quad (\text{B.2})$$

where $\theta \in [0, \pi]$.

$$r_i(r, \theta) = \sqrt{(Z_H - Z_I - r \cos \theta)^2 + r^2 \sin^2 \theta} \quad (\text{B.3})$$

$$\theta_i(r, \theta) = \arctan \frac{r \sin \theta}{Z_H - Z_I - r \cos \theta} \quad (\text{B.4})$$

where $\theta \in [0, \pi]$.

The matrix elements we need to evaluate are in the form

$$V_{ij}^2(\Theta) = e^{-i\Theta} \int r_i^2 dr_i \int d\theta_i \sin \theta_i \int d\phi_i \dots \quad (\text{B.5})$$

Using $\xi_i = \cos \theta_i$ and $\xi = \cos \theta$ in above equations, we obtain

$$r(r_i, \theta_i) = \sqrt{(Z_H - Z_I + r_i \xi_i)^2 + r_i^2 (1 - \xi_i^2)}$$

$$\begin{aligned}
&= \sqrt{(Z_H - Z_I)^2 + 2(Z_H - Z_I)r_i\xi_i + r_i^2\xi_i^2} + r_i^2 - r_i^2\xi_i^2 \\
&= \sqrt{(Z_H - Z_I)^2 + 2(Z_H - Z_I)r_i\xi_i + r_i^2}
\end{aligned}$$

$$r \cos \theta = Z_H - zI + r_i \cos \theta_i$$

$$Z_H - r\xi = Z_I - \xi_i r_i$$

$$\xi(r_i, \theta_i) = \frac{Z_H - Z_I + \xi_i r_i}{r}$$

$$r(r_i, \theta_i) = \sqrt{(Z_H - Z_I)^2 + 2(Z_H - Z_I)r_i\xi_i + r_i^2} \quad (\text{B.6})$$

$$\xi(r_i, \theta_i) = \frac{Z_H - Z_I + \xi_i r_i}{r} \quad (\text{B.7})$$

Appendix C

Impurity basis-function set

C.1 Definition of the basis set

The basis-functions on the impurity consist of the radial part and the angular part. The angular part is the spherical harmonic for various m values, and the radial part is a generalized Laguerre polynomial with an exponential weight factor. We make our polynomials functions of $r\lambda_I$ instead of only radial distance to make our normalizations easier. Our normalization coefficient is a function of λ .

$$\Psi_{I,\ell,n,m} = C(\lambda_I)(r_I\lambda_I)^\ell e^{-\frac{\lambda_I}{2}r_I} L_n^{2\ell+2}(\lambda_I r_I) P_{\ell,m}(\cos(\theta)) \quad (C.1)$$

By defining $x = \lambda_I r_I$, we can write our basis-functions as

$$\Psi_{I,\ell,n,m} = C(\lambda_I)x^\ell e^{-\frac{x}{2}} L_n^{2\ell+2}(x) P_{\ell,m}(\cos(\theta)) \quad (C.2)$$

We calculate $\langle \Psi_I | \Psi_I \rangle$ in order to find the coefficients as follows,

$$1 = C(\lambda_I)^2 \int d\vec{r} \Psi_{I,\ell,n,m} \Psi_{I,\ell,n,m} \quad (C.3)$$

$$\begin{aligned} 1 &= C(\lambda_I)^2 \int r^2 dr \int d\cos(\theta) \Psi_{I,\ell_1,n_1,m_1} \Psi_{I,\ell_2,n_2,m_2} \\ &= \frac{C(\lambda_I)^2}{\lambda^3} \int x^2 dx \Psi_{I,\ell_1,n_1,m_1} \Psi_{I,\ell_2,n_2,m_2} \delta_{\ell_1,\ell_2} \delta_{m_1,m_2} \end{aligned}$$

$$\begin{aligned}
\frac{\lambda_I^3}{C(\lambda_I)^2} &= \int x^2 dx \Psi_{I_{R,\ell_1,n_1}} \Psi_{I_{R,\ell_1,n_1}} \delta_{l_1,l_2} \delta_{m_1,m_2} \\
\frac{\lambda_I^3}{C(\lambda_I)^2} &= \int dx e^{-x} x^{\ell_1+\ell_2+2} \mathbb{L}_{n_1}^{2\ell_1+2}(x) \mathbb{L}_{n_2}^{2\ell_2+2}(x) \delta_{l_1,l_2} \delta_{m_1,m_2} \\
\frac{\lambda_I^3}{C(\lambda_I)^2} &= \int dx e^{-x} x^{2\ell+2} \mathbb{L}_{n_1}^{2\ell+2}(x) \mathbb{L}_{n_2}^{2\ell+2}(x) \delta_{l_1,l_2} \delta_{m_1,m_2} \\
\frac{\lambda_I^3}{C(\lambda_I)^2} &= (n+1)(n+2) \cdots (n+2\ell+2) \\
C(\lambda_I) &= \sqrt{\frac{\lambda_I^3}{(n+1)(n+2) \cdots (n+2\ell+2)}} \tag{C.4}
\end{aligned}$$

where $\Psi_{I_{R,\ell,n,m}}$ is the radial part of the basis-function and we use the orthonormality condition of spherical basis-functions for different ℓ and m values.

C.2 Derivative of the radial part of the impurity basis-functions

$$\begin{aligned}
\Psi_{I_{R,\ell_1,n_1}} &= C_{R,n,l} x^\ell e^{-\frac{x}{2}} \mathbb{L}_n^{2\ell+2}(x) \\
\frac{\partial}{\partial r} &= \lambda_I \frac{\partial}{\partial x} \left[C_{R,n,l} x^\ell e^{-\frac{x}{2}} \mathbb{L}_n^{2\ell+2}(x) \right] \\
&= C_{R,n,l} \lambda_I \left[\ell x^{\ell-1} e^{-\frac{x}{2}} \mathbb{L}_n^{2\ell+2}(x) - \frac{1}{2} x^\ell e^{-\frac{x}{2}} \mathbb{L}_n^{2\ell+2}(x) + x^\ell e^{-\frac{x}{2}} \frac{\partial}{\partial x} \mathbb{L}_n^{2\ell+2}(x) \right] \\
&= C_{R,n,l} \lambda_I x^\ell e^{-\frac{x}{2}} \left[\left(\frac{\ell}{x} - \frac{1}{2} \right) \mathbb{L}_n^{2\ell+2}(x) + \frac{\partial}{\partial x} \mathbb{L}_n^{2\ell+2}(x) \right] \\
&= \lambda_I \left[\Psi_{I_{R,\ell_1,n_1}} \left(\frac{\ell}{x} - \frac{1}{2} \right) + C_{R,n,l} x^\ell e^{-\frac{x}{2}} \frac{\partial}{\partial x} \mathbb{L}_n^{2\ell+2}(x) \right] \tag{C.5}
\end{aligned}$$

C.3 Derivatives of the Impurity basis-functions w.r.t. Hydrogen center

$$r_I^2 = r^2 + d^2 - 2rd \cos(\theta) \tag{C.6}$$

$$\begin{aligned}
2r_I \frac{\partial r_I}{\partial r} &= 2r - 2d \cos(\theta) \\
\frac{\partial r_I}{\partial r} &= \frac{r - d \cos(\theta)}{r_I} \\
&= \frac{r - dz}{r_I}
\end{aligned} \tag{C.7}$$

$$\begin{aligned}
2r_I \frac{\partial r_I}{\partial \theta} &= 2rd \sin(\theta) \\
\frac{\partial r_I}{\partial \theta} &= \frac{rd \sin(\theta)}{r_I}
\end{aligned} \tag{C.8}$$

$$\begin{aligned}
\frac{1}{r} \frac{\partial r_I}{\partial \theta} &= \frac{d \sin(\theta)}{r_I} \\
\frac{1}{r} \frac{\partial r_I}{\partial \theta} &= \frac{d(1 - z^2)^{\frac{1}{2}}}{r_I}
\end{aligned} \tag{C.9}$$

$$\theta_I = \tan^{-1} \frac{-r \sin(\theta)}{d - r \cos(\theta)} \tag{C.10}$$

$$\begin{aligned}
\frac{\partial \theta_I}{\partial r} &= \frac{1}{1 + \frac{r^2 \sin^2(\theta)}{(d - r \cos(\theta))^2}} \frac{\partial}{\partial r} \left(\frac{-r \sin(\theta)}{d - r \cos(\theta)} \right) \\
&= \frac{-(d - r \cos(\theta))^2 - \sin(\theta) [d - r \cos(\theta) + r \cos(\theta)]}{d^2 + r^2 - 2dr \cos(\theta) (d - r \cos(\theta))^2} \\
&= \frac{-d \sin(\theta)}{r_I^2} \\
&= \frac{-d(1 - z^2)^{\frac{1}{2}}}{r_I^2}
\end{aligned} \tag{C.11}$$

$$\begin{aligned}
\frac{\partial \theta_I}{\partial \theta} &= \frac{1}{1 + \frac{r^2 \sin^2(\theta)}{(d - r \cos(\theta))^2}} \left[\frac{r \cos(\theta)(d - r \cos(\theta)) - r \sin(\theta)(r \sin(\theta))}{(d - r \cos(\theta))^2} \right] \\
&= \frac{rd \cos(\theta) - r^2(\sin^2(\theta) + \cos^2(\theta))}{r_I^2} \\
&= \frac{rd \cos(\theta) - r^2}{r_I^2}
\end{aligned} \tag{C.12}$$

$$\frac{1}{r} \frac{\partial \theta_I}{\partial \theta} = \frac{d \cos(\theta) - r}{r_I^2} \tag{C.13}$$

Appendix D

Calculation of Hamiltonian

Calculation of $V_{ij}^{(1)}(\Theta)$

We can write this matrix element as follows.

$$V_{ij}^{(1)}(\Theta) = \int d\vec{r} \Psi_i(\vec{r}) V(re^{i\Theta}, \Omega) \Psi_j(\vec{r}) \quad (D.1)$$

$$\begin{aligned} &= e^{-i\Theta} C_i(\lambda) C_j(\lambda) \int dr e^{-\lambda r e^{-i\Theta}} \chi_i(\lambda r e^{-i\Theta}) \chi_j(\lambda r e^{-i\Theta}) \\ &\quad \times \int d\theta \sin \theta P_{li}(\cos \theta) P_{lj}(\cos \theta) V(r, \theta) \end{aligned} \quad (D.2)$$

$$\begin{aligned} &= e^{-i\Theta} C_i(\lambda) C_j(\lambda) \int dr e^{-\lambda_R r} e^{-i\lambda_I r} \chi_i(\lambda r e^{-i\Theta}) \\ &\quad \times \chi_j(\lambda r e^{-i\Theta}) S_{li,lj}(r) \end{aligned} \quad (D.3)$$

where

$$S_{li,lj}(r) = \int d\theta \sin \theta P_{li}(\cos \theta) P_{lj}(\cos \theta) V(r, \theta) \quad (D.4)$$

$$\begin{aligned} V_{ij}^{(1)}(\Theta) &= \frac{e^{-i\Theta} C_i(\lambda) C_j(\lambda)}{\lambda_R} \int dr e^{-r} e^{\frac{i\lambda_I}{\lambda_R} r} \\ &\quad \chi_i\left(\frac{\lambda}{\lambda_R} r e^{-i\Theta}\right) \chi_j\left(\frac{\lambda}{\lambda_R} r e^{-i\Theta}\right) S_{li,lj}\left(\frac{r}{\lambda_R}\right) \end{aligned} \quad (D.5)$$

Using Gauss Theorem we obtain

$$V_{ij}^{(1)}(\Theta) = \frac{e^{-i\Theta} C_i(\lambda) C_j(\lambda)}{\lambda_R} \sum_{k=1}^{Nk} W_k \left[e^{\frac{i\lambda_I}{\lambda_R} r_k} \chi_i\left(\frac{\lambda}{\lambda_R} r_k e^{-i\Theta}\right) \chi_j\left(\frac{\lambda}{\lambda_R} r_k e^{-i\Theta}\right) S_{l_i l_j}\left(\frac{r_k}{\lambda_R}\right) \right] \quad (D.6)$$

We define pseudo basis-functions

$$\tilde{\Psi}_i(r_k) = \frac{C_i(\lambda)}{\sqrt{\lambda_R}} \sqrt{W_k} e^{i\frac{\lambda_I}{2\lambda_R} r_k} \chi_i\left(\frac{\lambda}{\lambda_R} r_k e^{-i\Theta}\right) \quad (D.7)$$

$$= C_i(\lambda) \sqrt{\frac{W_k}{\lambda_R}} e^{i\frac{\tan \Theta}{2} r_k} \chi_i\left(\frac{r_k}{\cos \Theta} e^{-i\Theta}\right) \quad (D.8)$$

and

$$V_{ij}^{(1)}(\Theta) = e^{-i\Theta} \sum_{k=1}^{Nk} \tilde{\Psi}_i(r_k) \tilde{\Psi}_j(r_k) S_{l_i l_j}\left(\frac{r_k}{\lambda_R}\right) \quad (D.9)$$

Calculation of $V_{ij}^{(2)}(\Theta)$

We can write this matrix element as follows.

$$V_{ij}^{(2)}(\Theta) = \int d\vec{r} \Psi_i(\vec{r}) V^{(2)}(r e^{i\Theta}, \Omega) \Psi_j(\vec{r}) \quad (D.10)$$

$$\begin{aligned} &= e^{-i3\Theta} C_i(\lambda) C_j(\lambda) \int dr_I r_I^2 \int d\theta_I \sin \theta_I e^{-\lambda r(r_I, \theta_I) e^{-i\Theta}} \\ &\quad \times \frac{\chi_i(\lambda r(r_I, \theta_I) e^{-i\Theta}) \chi_j(\lambda r(r_I, \theta_I) e^{-i\Theta})}{[r(r_I, \theta_I) e^{-i\Theta}]^2} \\ &\quad \times P_{l_i}(\cos \theta(r_I, \theta_I)) P_{l_j}(\cos \theta(r_I, \theta_I)) V^{(2)}(r_I, \theta_I) \end{aligned} \quad (D.11)$$

Lets define pseudo basis-functions as follows

$$\bar{\Psi}_i(r_I, \theta_I) = r_I \frac{C_i(\lambda)}{r(r_I, \theta_I)} e^{-\frac{\lambda}{2} r(r_I, \theta_I) e^{-i\Theta}} \chi_i(\lambda r(r_I, \theta_I) e^{-i\Theta}) P_i(\cos \theta(r_I, \theta_I)) \quad (\text{D.12})$$

and if we make change of variables in the angular integration $\xi_i = \cos \theta_I$ we obtain

$$V_{ij}^{(2)}(\Theta) = e^{-i\Theta} \int_0^{r_{cut}} dr_I \int_{-1}^1 d\xi \bar{\Psi}_i(r_I, \xi_I) V^{(2)}(r_I, \xi_I) \bar{\Psi}_j(r_I, \xi_I) \quad (\text{D.13})$$

Bibliography

- [1] W. Ho. Mechanisms for photodissociation and photodesorption of molecules adsorbed on solid surfaces. *Comments Cond. Mat. Phys.*, 13:293, 1988.
- [2] N. D. Lang. Ionization probability of sputtered atoms. *Phys. Rev. B*, 27:2019, 1983.
- [3] M. L. Yu and N. D. Lang. Direct evidence of electron tunneling in the ionization of sputtered atoms. *Phys. Rev. Lett.*, 50:127, 1983.
- [4] N. D. Lang, A. R. Williams, F. J. Himpsel, B. Reihl, and D. E. Eastman. *Phys. Rev. B*, 26:1728, 1982.
- [5] D. M. Newns. Charge transfer in atom-surface scattering. *Comments Cond. Mat. Phys.*, 14:295, 1989.
- [6] J. K. Nørskov, S. Holloway, and N. D. Lang. *Surf. Sci*, 137:65, 1984.
- [7] N. D. Lang, S. Holloway, and J. K. Nørskov. Electrostatic adsorbate-adsorbate interactions: The poisoning and promotion of the molecular adsorption reaction. *Surf. Sci.*, 150:24, 1985.
- [8] P. Nordlander and N.D. Lang. Energy shifts and broadening of atomic levels near impurity-covered metal surfaces. *Phys. Rev.*, B44:13681, 1991.

- [9] L. H. Thomas. *Proc. Cambridge Phil. Soc.*, 23:542, 1927.
- [10] P. Hohenberg and W. Kohn. *Phys. Rev.*, 136:B864, 1964.
- [11] W. Kohn and L. J. Sham. *Phys. Rev.*, 140:A1133, 1965.
- [12] D. Pines. *Elementary Excitations in Solids*. Benjamin, New York, 1963.
- [13] D. Pines. *Computational Methods in Band Theory*. Plenum, New York, 1971.
- [14] J. Rudnick. PhD thesis, University of California, San Diego, 1970.
- [15] E. Zaremba and W. Kohn. *Phys. Rev. B*, 15:1769, 1977.
- [16] P. Nordlander and J. Harris. *J. Phys. C*, 17:1141, 1984.
- [17] J. W. Gadzuk. Theory of atom-metal interactions. *Surf. Sci.*, 6:133, 1967.
- [18] M. Remy. Etude quantitative de la liaison de chimisorption: determination de l'enlargissement du niveau de valence d'un atome alcalin adsorbé. *Comptes Rendus*, 287:235, 1978.
- [19] P. Nordlander and J. C. Tully. Energy shifts and broadening of excited hydrogen-atom levels in the vicinity of a metal surface. *Phys. Rev. Lett.*, 61:990, 1988.
- [20] S. Ossicini, C. M. Bertoni, and P. Gies. Image plane for surface potential. *Europhys. Lett.*, 1:661, 1986.
- [21] O. Gunnarsson and R. O. Jones. Density functional calculations for atoms, molecules and clusters. *Phys. Scr.*, 21:394, 1980.
- [22] N. D. Lang and W. Kohn. *Phys. Rev. B*, 7:3541, 1973.

- [23] G. D. Mahan. *Many-Particle Physics*. Plenum, New York, 1990.
- [24] W. H. Press, B. P. Flannery, S. A. Teukolsky, and W. T. Wetterling. *Numerical Recipes*. Cambridge University Press, Cambridge, 1986.
- [25] W. P. Reinhardt. Complex coordinates in the theory of atomic and molecular structure and dynamics. *Annu. Rev. Phys. Chem.*, 33:223, 1982.
- [26] R. Yaris and P. Winkler. *J. Phys. B*, 11:1475, 1978.
- [27] P. Nordlander and J. C. Tully. *Phys. Rev. B*, 42:5564, 1990.